The Subseasonal North Atlantic Oscillation is a Quasi-Semiannual, Propagating Disturbance

Samuel Smith[1*], Jian Lu[2,3], and Paul W. Staten[4]

[1]Dept. of Geophysical Sciences, University of Chicago, Chicago, IL 60615

[2]Coll. of Oceanic and Atmospheric Sciences, Ocean University of China, Qingdao, China 266100

[3]Earth Sciences Division, Pacific Northwest National Laboratory, Richland, WA 99354

[4]Dept. of Earth and Atmospheric Sciences, Indiana University, Bloomington, IN 47405

*5734 S. Ellis Ave, Chicago, IL 60637; samuelsmith@uchicago.edu

Abstract

The North Atlantic Oscillation (NAO) is a well-studied mode of regional climate variability, associated with fluctuations in sea-level pressure (SLP), storm tracks, and the North Atlantic jet. These fluctuations have been perceived as a seesawing between two climatic phases, one corresponding to a more poleward jet and the other to a more equatorward. However, recent work has shown that zonal wind anomalies also propagate poleward at interseasonal timescales. Using reanalysis data, this work demonstrates for the first time that the subseasonal NAO propagates with a 145-day period, explaining the recently discovered long-term predictability of the NAO. This propagation period can be predicted from a reduced-order model of zonal wind dynamics. This propagating behavior is fundamental to the NAO, representing the true "dynamic mode" of North Atlantic jet variability, and removing this propagation in the reduced-order model decreases the NAO's predictability. Furthermore, the NAO's climate anomalies, including SLP, propagate along with the wind; SLP exhibits the same low-frequency periodicity as the wind. This suggests the NAO has two under-studied phases in quadrature with the "seesaw" phases. Finally, our work suggests that the North Atlantic response to uniform climate forcing will include both a poleward jet shift and a jet strengthening.

The North Atlantic Oscillation (NAO) is the dominant mode of climate variability for eastern North America and western Europe[1,2,3]. Traditionally, the NAO is viewed as a fluctuation in the strength and position of the Azores High and Icelandic Low pressure centers, accompanied by changes in the North Atlantic eddy-driven jet[3,4,5]. The NAO modifies temperature, precipitation, wind speed, sea ice, and sea surface temperature, controlling both regional climate and the manifestation of climate change[3,6,7,8,9]. The NAO has also been linked to climate extremes in North America, Europe, and Asia, as well as flood risk in Northern Europe and the associated economic damage[10,11,12,13].

However, the NAO's recent trends and its response to human emissions remain poorly understood[14,15,16,17]. The current generation of climate models predict a future strengthening of the NAO, while simultaneously failing to capture its historical strengthening, raising questions about their credibility[14,15,18,19,20,21]. Furthermore, the models underestimate the predictability of the NAO, a phenomenon known as the "signal-to-noise paradox"[11,15,22,23]. This "paradox" is that realistic GCMs forecast the observed NAO better than the same model's own NAO at long lead times[11]. Various (possibly overlapping) causes have been suggested for this "underestimated" predictability: problems with forecast initialization[15], non-ergodicity[24], non-Gaussianity[25,26], and underestimated midlatitude climate persistence[27,28,29].

Given these questions about the NAO's seasonal predictability and long-term response to climate forcings, which at first appear distinct, we propose a reduced-order model for North Atlantic climate: the stochastic, linear dynamical system, first applied to the climate system by Hasselmann[30], of the form

$$\frac{d\mathbf{u}}{dt} = \mathbf{A}\mathbf{u} + \mathbf{f}\,. \qquad (1)$$

Here, $\mathbf{u}$ is the state vector; $\mathbf{A}$, the "dynamics", is a linear operator which describes how the state vector evolves temporally; and $\mathbf{f}$ is a (possibly stochastic) forcing. For the NAO, $\mathbf{u}$ might be SLP, surface streamfunction, or zonal wind. $\mathbf{f}$ is not purely "external" forcing; some portion is also the induced or "Eliassen" response[31].

To illustrate the value of (1), consider two limiting cases. In the first, the system is unforced ($\mathbf{f} = \mathbf{0}$), and thus (1) is solved for an initial value as $\mathbf{u}'(t) = \mathbf{u}'(0)e^{\mathbf{A}t}$, where the prime represents deviations from the time mean. If $\mathbf{A}$ is diagonalizable by its eigenvectors $\mathbf{v}_i$, $\mathbf{u}'$ evolves linearly with $\mathbf{V}e^{\mathbf{\Lambda}t}\mathbf{V}^{-1}$, where $\mathbf{v}_i$ form the columns of $\mathbf{V}$ and $\mathbf{\Lambda}$ is a diagonal matrix of the eigenvalues λ_i. This means that the eigenvectors of $\mathbf{A}$, the "modes of variability", represent fundamental modes of $\mathbf{u}$ with a timescale determined by the eigenvalues λ_i. $\mathbf{A}$ is real, and so λ_i will either be real or in complex conjugate pairs; the inverse real component determines the mode's e-folding timescale and any imaginary component determines the mode's frequency.

The eigenvalues of $\mathbf{A}$ also determine the predictability of (1). The initial value case above represents the best linear prediction for (1), even with nonzero $\mathbf{f}$. In the idealized case of perfect prediction and observing systems (determining the theoretical limit), the prediction error $\mathbf{u_{obs}} - \mathbf{u}(0)e^{\mathbf{A}t}$ evolves like (1) and the prediction error covariance at forecast lead τ, $\mathbf{C}(\tau)$, obeys

$$\mathbf{C}(\tau) = \mathbf{C}(\infty) - \mathbf{V}e^{\mathbf{\Lambda}\tau}\mathbf{V}^{-1}\mathbf{C}(\infty)\mathbf{V}^{-1}e^{\mathbf{\Lambda}\tau}\mathbf{V}\,. \qquad (2)$$

Here $\mathbf{C}(\infty)$ is the climatological error covariance (eq. 13 in Tippet and Chang[32]). Smaller $\mathbf{C}(\tau)$ and thus smaller $e^{\mathbf{\Lambda}\tau}$ means greater predictability. Therefore, the least-damped eigenvector $\mathbf{v_i}$ corresponds to the most predictable mode of $\mathbf{u}$[33].

The second illustrating case for (1) is where $\mathbf{u} = \bar{\mathbf{u}}$ (its time-mean value), and thus $\frac{\partial \bar{\mathbf{u}}}{\partial t} = \mathbf{0}$. If the operator $\mathbf{A}$ is nonsingular, the solution of (1) is $\bar{\mathbf{u}} = -\mathbf{A}^{-1}\mathbf{f}$, which implies $\mathbf{V}^{-1}\bar{\mathbf{u}} = -\lambda_i^{-1}\mathbf{V}^{-1}\mathbf{f}$. If the forcing is uniformly distributed across modes of $\mathbf{A}$, then the forced $\bar{\mathbf{u}}$ projects onto its modes of variability proportionally to their damping timescales. This is a statement of the "fluctuation-dissipation theorem" (FDT) for this system. Since its introduction to climate science[34], FDT has been applied to predict the atmospheric response to weak forcing with varying levels of success[32,35,36,37,38,39,40,41].

While these two limiting cases are idealized, they illustrate the insight available in (1). If the FDT holds qualitatively for the NAO, it would have serious implications for current climate projections. The leading mode of zonal-mean zonal wind variability in the Northern Hemisphere, the Northern Annular Mode (NAM), is too transient (or only adequately so) during NH winter in a range of CMIP and subseasonal forecast models[29,42,43]. Because the NAO and NAM are akin[4,44], models may be underestimating future changes in the North Atlantic jet. Assuming models are not missing a source of low-frequency variability, this is consistent with recent findings that current NAO trends exceed most model predictions[14].

Past attempts to model the NAO using (1) have assumed that $\mathbf{A}$ is diagonal in EOF-space, reducing it to a constant feedback parameter[45]. This is not justified because EOFs, while explaining the maximum variance, are not generally the eigenvectors of $\mathbf{A}$[33,46,47,48,49,50]. Additionally, the Southern Annular Mode (SAM) – the NAO's Southern Hemisphere cousin – cannot be explained with diagonal dynamics. The SAM has recently been shown to have interactions between its first and second EOFs that produce a 150-day meridional propagation of zonal wind anomalies[37,51,52].

Using reanalysis data, this work addresses whether (1) is a suitable conceptual model for the North Atlantic jet and what its dominant mode of variability is. We ask whether the NAO exhibits a meridional propagation like the SAM, and what the implications of this propagation are for short-term forecasting, for predictability, and for the forced response. The meridional propagation of zonal-mean momentum anomalies has recently been found to influence the NAO at seasonal-to-annual timescales[53,54], but the current work will show that this propagation is the NAO itself.

1. Results

1.1. Theory of Variability for Regional Jets

In column-integrated, zonal-mean, quasi-geostrophic theory, the zonal momentum equation is a balance between the eddy momentum flux convergence (EMFC), which drives the jets, and surface drag, which slows them. For a regional-mean, this balance is modified by "boundary effects". However, if a longitudinal sector $\Delta\lambda$ contains a wave source whose zonal length scale is considerably greater than its meridional scale, as for the North Atlantic, the boundary effects can be neglected[4] (see Supplemental Section 1). Thus, the approximate regional balance is the same:

$$\partial_t[\langle u\rangle]_{\Delta\lambda} \approx [\langle M\rangle]_{\Delta\lambda} + [X_s]_{\Delta\lambda}. \quad (3)$$

Here M is the EMFC, u is zonal momentum, X_s is surface friction, $[\,\cdot\,]_{\Delta\lambda}$ is the sectoral average, and $\langle\,\cdot\,\rangle$ is the (mass-weighted) column average.

Given the simplicity of (3), can it be expressed as a linear dynamical system (1)? Classically, friction is assumed to be a linear Rayleigh drag[4,55], or $[X_s]_{\Delta\lambda} \approx$

$-r(\phi)[\langle u\rangle]_{\Delta\lambda}$, where $r(\phi)$ is the damping rate and ϕ is latitude. We validate our approximations for the NAO in Supplemental Figures 1, 2, and 3.

The next task, connecting the EMFC $[\langle M\rangle]_{\Delta\lambda}$ with mean flow $[\langle u\rangle]_{\Delta\lambda}$, is a longstanding challenge[35,37,55,56]. For now, assume it has a linear response $\mathbf{M}(\phi)[\langle u\rangle]_{\Delta\lambda}$ (the "eddy feedback") with an additional stochastic component $\widetilde{M}(\phi)$, independent of $[\langle u\rangle]_{\Delta\lambda}$ and driven by high-frequency eddies. If so, we can write (3) as (1)

$$\partial_t[\langle u\rangle]_{\Delta\lambda} \approx (\mathbf{M} - r)[\langle u\rangle]_{\Delta\lambda} + \widetilde{M} \stackrel{\text{def}}{=} \mathbf{A}[\langle u\rangle]_{\Delta\lambda} + \widetilde{M}\,. \tag{4}$$

The subject of how to estimate $\mathbf{M}$ for the midlatitude westerlies has been studied extensively[35,37,40,55].

Using the EOF basis vectors, one can project (4) onto this basis:

$$\frac{d\boldsymbol{z}}{dt} = (\mathbf{B} - \mathbf{T}^{-1})\boldsymbol{z} + \widetilde{\boldsymbol{m}}\,. \tag{5}$$

Here, $\boldsymbol{z}$ represents the EOF timeseries (the first being an index for the NAO), $\mathbf{B}$ the eddy feedback matrix, $\mathbf{T}^{-1}$ the (diagonal) damping rate matrix, and $\widetilde{\boldsymbol{m}}$ the stochastic forcing. Thus, (5) is a multi-dimensional, regional extension of the Lorenz-and-Hartmann model for the SAM[55] and NAM[57]. Note that (5) does not require the dynamics ($\mathbf{B}$) to be diagonal in EOF space[51], although this has been frequently assumed[45,55,57]. It does require that each mode is forced independently. Equations (4) and (5) represent the linear dynamical systems we analyze for the NAO. Hereafter, we interpret the leading modes of (4) and (5) as the NAO, extending the traditional SLP-based definition.

1.2. Propagation of the Subseasonal NAO

The subseasonal NAO exhibits all the features of propagating modes in EOF space[40]: the two leading modes (NAO1 and NAO2) decay at similar rates, explain

similar fractions of the variance, and gradually follow one another in time (see Supplemental Figures 4 and 5). Because of this evidence for propagation, we use (5), the cross-EOF feedback model of Lubis and Hassanzadeh[51], hereafter LH20, to determine the strength of the eddy-jet feedback and the period and decay timescale for the propagation (Table 1).

b_{11}	b_{12}	b_{21}	b_{22}
0.052±0.004	0.035±0.019	-0.061±0.004	0.019±0.030
τ_1^{-1}	τ_2^{-1}	σ^{-1}	$\mathcal{T}$
7.2±0.6	7.3±0.9	-9.7±2.1	144±47

Table 1: Cross-EOF feedback parameters ($b_{11}, b_{12}, b_{21}, b_{22}$) computed from the two leading EOFs (NAO1 and NAO2) of North-Atlantic-mean, vertically integrated zonal wind in MERRA2 from 1980-2023. Units are days^{-1}. Feedbacks are computed across lag days 7-18 and averaged, as in LH20. The frictional damping timescales (τ_1, τ_2) are estimated using the method outlined in Lorenz & Hartmann (2001), Appendix A. They have units of days. See Section 3.1 for details. Period ($\mathcal{T}$) and decay timescale (σ^{-1}) are estimated using (6) and (7), respectively, and also have units of days. Ranges are estimated using a bootstrapping technique outlined in Section 3.1; they represent one-half the inner-quartile range for the estimated distributions.

Table 1 provides further evidence of propagation: the eigenvalue solution to (5) is complex (i.e., $\mathcal{T} \neq 0$). Note that EOF1-EOF2 interaction, represented by nonzero b_{ij}, does not guarantee propagation; $(\mathbf{B} - \mathbf{T^{-1}})$ is real and could have purely real eigenvalues. The fact that it does not is evidence that the mode is propagating[51,58]. Additionally, the propagation period is nearly 150 days – the same periodicity that has been observed for SAM[52].

Since the NAO's dynamics are propagating and not diagonal in EOF-space, we must consider whether the true dynamic modes of North-Atlantic zonal wind variability are different from the EOFs[49]. Therefore, we use dynamic mode decomposition (DMD; see Section 3.2) to estimate the true modes (eigenvectors) of (3) without the linear

assumption of (4). Despite this, DMD modes still obey (5). See Section 3.2 and Schmid [59] for a recent review.

The three least-damped DMD modes of zonal wind correspond to the three most predictable and most excitable modes (Figure 1). The wind anomalies reconstructed from these three modes have a spatiotemporal correlation of about 0.70 with the original anomalies, representing a substantial fraction of the variability. The decay scale of the first leading mode is 8.1 days, much longer than the others (3.2 and 2.8 days), and its correlation is 0.66 with the original data. Thus, the first mode dominates. It is complex (i.e., propagating) with a period of 146.3 days, consistent with the prediction from the LH20 model (Table 1). Further, it has a spatial correlation of 0.95 with the complex $\mathrm{EOF1} + i\,\mathrm{EOF2}$. This validates that EOF1 and EOF2 capture two components of a physical, propagating mode – the NAO.

We have confidence this mode is physical and not a statistical artefact (cf. Gerber and Thompson[50]). While not previously identified in the North Atlantic, meridional propagation of zonal wind anomalies has been recognized at a global scale for decades[60,61,62], and the propagation mechanism has been explained using theories of wave-mean-flow interaction. Essentially, a dipolar zonal wind anomaly drifts poleward because negative zonal wind anomalies enhance the breaking of midlatitude waves on their poleward flank. This decelerates the wind along this flank and converges momentum on the poleward flank of the positive anomaly, effectuating a poleward shift of the dipole. See Lee et al.[60] and Lorenz[63] for greater detail.

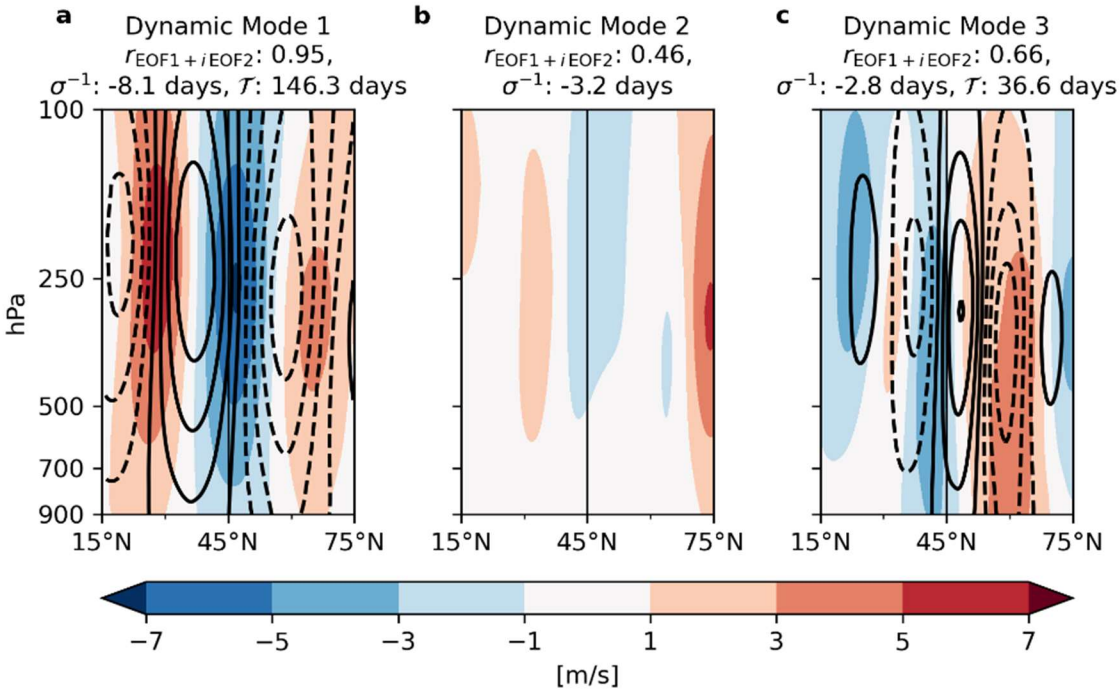

Figure 1: The three least-damped dynamic modes of North-Atlantic-mean zonal wind in MERRA2 (1980-2023). The shading is the real component and the contours are the imaginary. The 2D pattern correlation with the complex $EOF1 + i\,EOF2$ vector, the inverse real part of the eigenvalue (damping timescale), and 2π times the inverse imaginary part of the eigenvalue (periodicity) are given above each mode. The modes are normalized such that the magnitude of the complex timeseries for each mode has unit variance, with the real part corresponding to phase angle of 0° and the imaginary part corresponding to 90°.

Notably, the vertical structure of DMD1 is strongly barotropic, which agrees with barotropic annular mode theory and the mechanism for meridional propagation[60,63,64]. The barotropic structure is also consistent with fluctuations in atmospheric mass and thus, sea-level pressure (SLP), the traditional measure used for the North Atlantic Oscillation. This suggests the SLP anomalies likely migrate with zonal wind anomalies.

If such periodicity of the zonal wind (and SLP) exists, it should appear in their power spectra. Because the mode is damped faster than its periodicity, and because

zonal wind anomalies often propagate with different speeds at different latitudes[63], any spectral peaks may be subtle. To retain the entire signal, we examine the power spectra in latitude-frequency space, normalizing the power by the variance at each latitude (Figure 3). Both zonal wind and SLP have red spectra[30], with the power decreasing with frequency, but they have notable peaks around the predicted propagation period (~150 days), which are statistically different from a red noise spectrum at the 90% confidence level (Figure 3, absence of hatching). Both zonal wind and SLP show significant peaks spread around the predicted period from 30°-60°N.

This quasi-semiannual periodicity agrees with and helps interpret the long-range predictability found in subseasonal forecasts[53,54]. The forecast models predict the hemispheric-mean momentum anomalies with a correlation above 0.5 for around 6 months (~1 period), with significant correlations out to 12 months[53]. Considering the tripolar structure of the mode in the extratropics (Figure 1a), this would require 1.5 periods (~8 months) for anomalies originating in the tropics to reach the poles. Notably, the annual predictability[53,54] is likely due to ENSO's steady forcing of the anomalies[65], but the propagation is due to internal atmospheric dynamics and not ENSO[53,54,60].

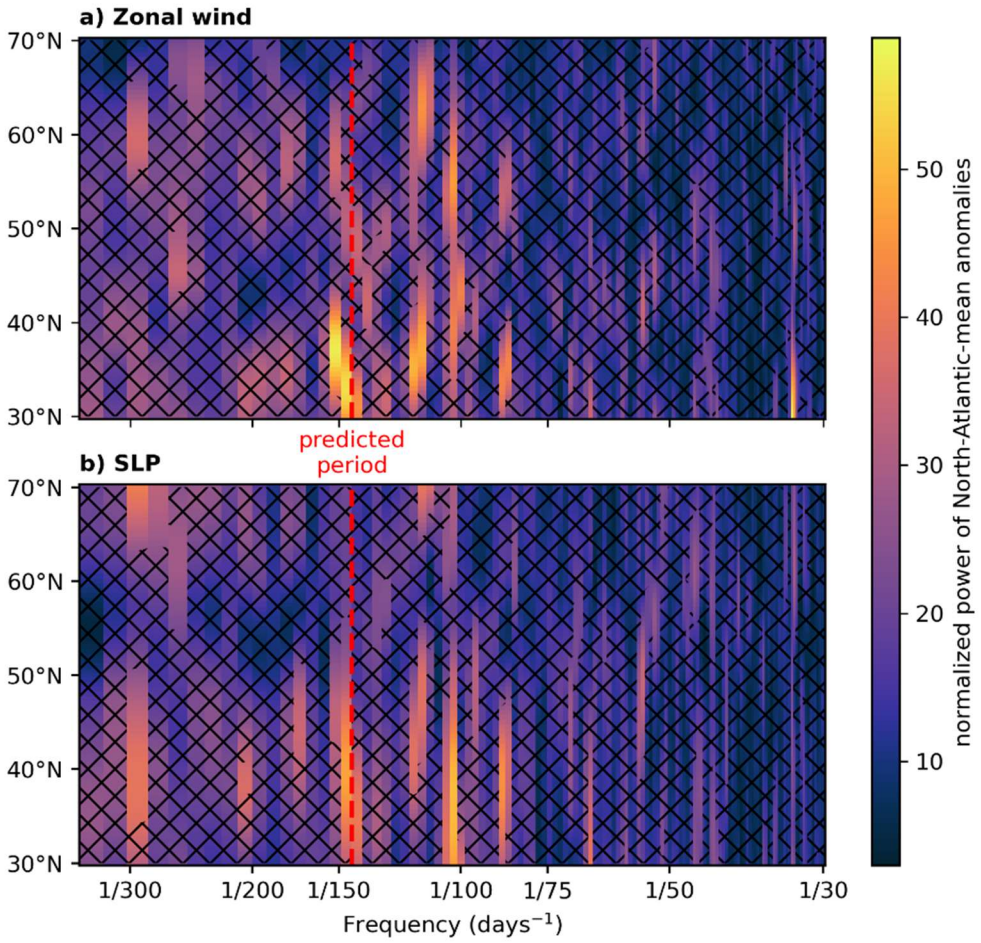

209

Figure 2: Power spectral density of North-Atlantic-mean (top) vertically-averaged zonal wind anomalies and (bottom) sea-level pressure (SLP) anomalies for 1980-2023. Power spectra are normalized by the variance of each latitude. Hatched areas are statistically indistinguishable from red noise at the 90% confidence level. See Section 3.3 for details.

210

211 *1.3. Impacts of the Propagating NAO*

212 We conclude our analysis by showing that the NAO's propagation has

213 implications for its surface climate anomalies and its overall predictability. Using the

214 phase of the DMD index (see Section 3.2) during the strongest propagating season

(October-March), we composite 15-day low-pass-filtered surface climate anomalies (Figure 3). In the composites, surface temperature, SLP, precipitation, and sea-surface temperature (SST) anomalies all propagate following the zonal wind anomalies. Propagation remains when we include high-frequency and year-round data, but the robustness decreases. The seasonality is consistent with zonal wind anomalies excited by ENSO in NH autumn and with the preference of propagation for separated eddy-driven and subtropical jets[54,60,66,67]. We independently verify the poleward migration of climate impacts by regressing the EOF1 and EOF2 indices against the surface climate anomalies, which shows that the modes' surface impacts are in quadrature (Supplemental Figure 6). Given that one mode often follows the other (Supplemental Figure 4), this further demonstrates that the surface anomalies propagate with zonal wind anomalies.

Despite finding SST anomalies which propagate following the NAO, it is unlikely that the North Atlantic ocean is the driver of this low-frequency atmospheric variability. This is because propagation occurs in models without any ocean[60,63] and these anomalies lag the NAO's evolution by two weeks. However, we cannot rule out all oceanic influence. Deeper investigation of potential NAO-SST feedbacks should be a subject of future work.

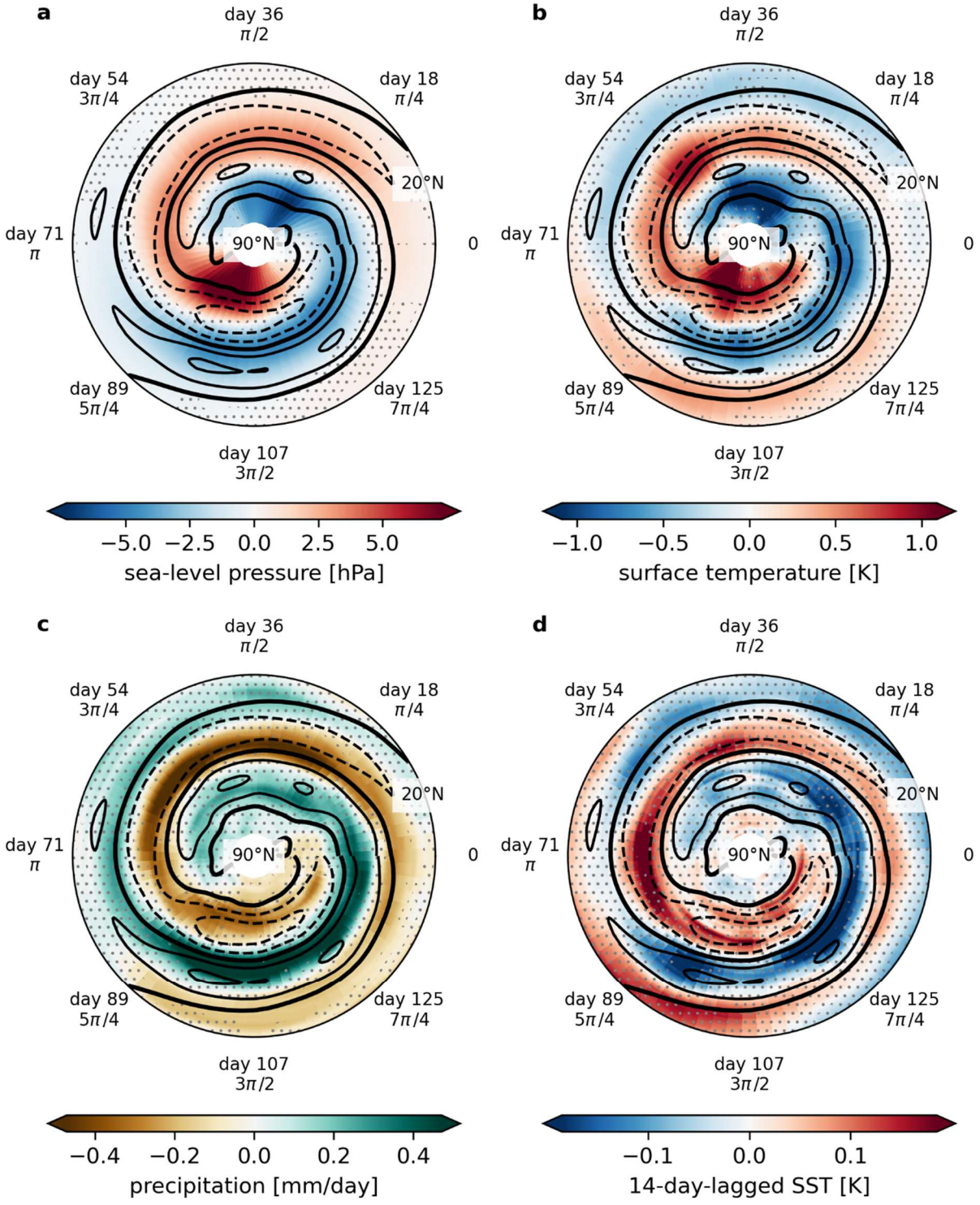
a
b
c
d
day 36
π/2
day 54
3π/4
day 18
π/4
day 71
π
0
day 89
5π/4
day 125
7π/4
day 107
3π/2
20°N
90°N
−5.0 −2.5 0.0 2.5 5.0
sea-level pressure [hPa]
−1.0 −0.5 0.0 0.5 1.0
surface temperature [K]
−0.4 −0.2 0.0 0.2 0.4
precipitation [mm/day]
−0.1 0.0 0.1
14-day-lagged SST [K]

Figure 3: NAO composites of the zonal-mean (100°W-30°E), anomalous (a) sea-level pressure, (b) surface temperature, (c) precipitation, and (d) lagged sea-surface temperature (SST) during October-March in MERRA2 (1980-2023). Daily anomalies are composited based on the phase of the 15-day-lowpass-filtered DMD index, binned every 5°. SST anomalies are at a 14-day lag. The contours show the composited westerly wind anomalies at 2 m/s intervals, with 0 m/s as the thick line. The periodicity is about 150 days/360°, shown along the top. Stippling indicates where fewer than 2/3 of the composite events agree on the sign.

Because the NAO is highly predictable[53], we examine how the propagation of the NAO influences this predictability. Using the perfect linear prediction framework[32], we compare how the "predictable information" (8), or predictability limit, varies between propagating and non-propagating regimes. Using a reduced-order, stochastic model of the NAO based on MERRA2 data (Table 1), we estimate the predictability of the propagating NAO and compare that to the predictability of the "classical", non-propagating assumption (Figure 4), $\mathbf{B}_{\mathrm{diag}} = \begin{bmatrix} b_{11} & 0 \\ 0 & b_{22} \end{bmatrix}$, where $b_{11} = 0.044 \pm 0.004$ days^{-1} and $b_{21} = 0.010 \pm 0.034$ days^{-1}. $\mathbf{B_{diag}}$ is estimated using (5) with $b_{12} = b_{21} = 0$.

A subtle but critical detail is that the e-folding timescales of EOF1 and EOF2 are identical in both cases. Thus, it is not obvious whether the predictability should differ. However, the predictability is significantly lower; both in the theoretical limit (Figure 4a) and in practice (Figure 4b). This is because 1) the coupling between EOF1 and EOF2 produces a mode with a slower decay rate ($\sigma^{-1} = 9.7$ days) and 2) the asymmetric cross-feedbacks induce correlations in the forcing, even though each EOF is forced independently. We disentangle these effects in Supplementary Figure 7a. Thus, in the propagating case, the NAO is more predictable, with ~30% more predictive information available at a 28-day forecast lead (note the log-scale in Figure 4).

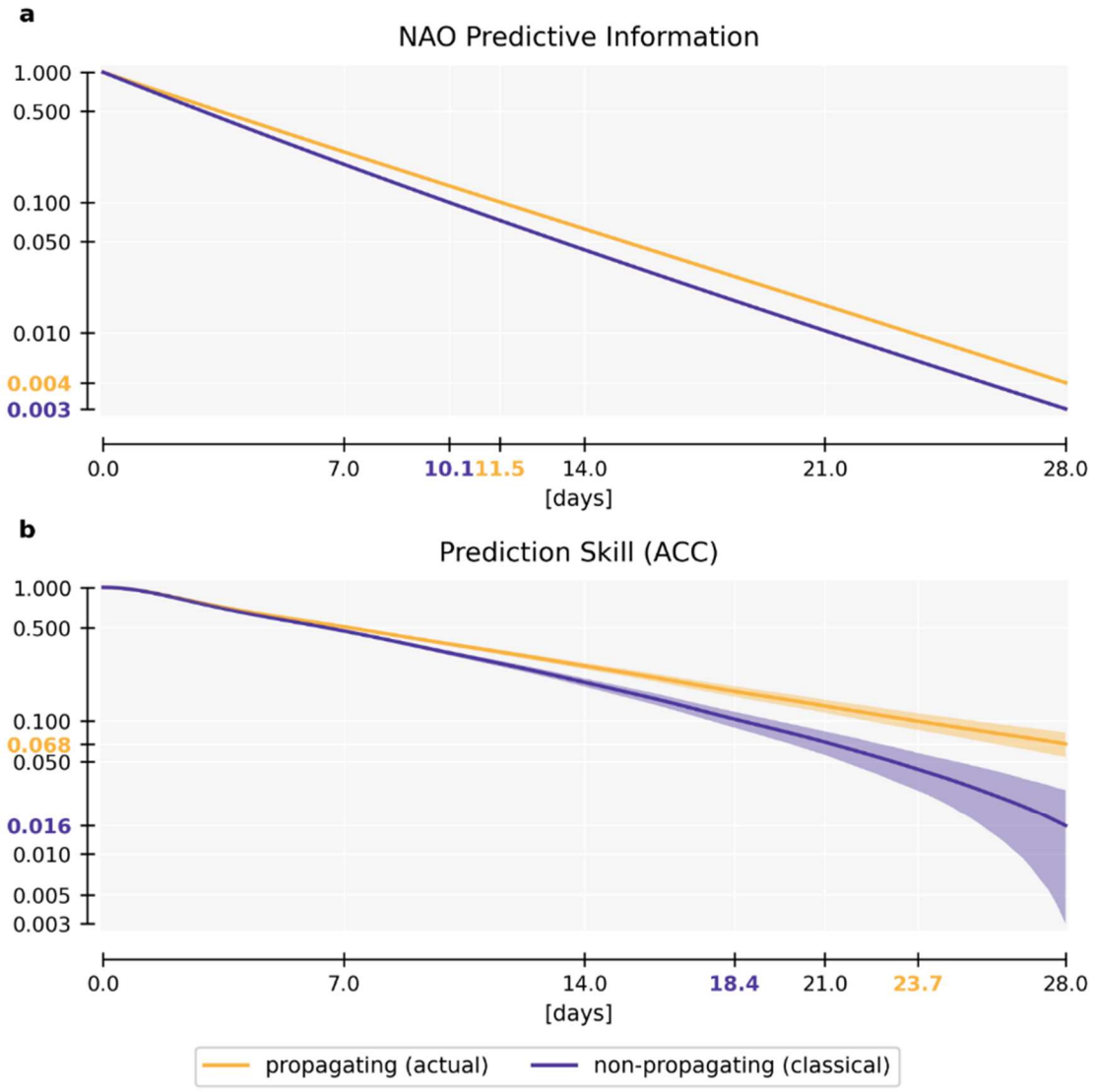

Figure 4: (a) The amount of predictive information (8) at various lead times in simulations of a stochastic model of the NAO for two different scenarios. The first uses the actual parameters fit from MERRA2 (including propagation); the other uses parameters with cross-EOF feedbacks set to 0 (no propagation) and a new $\mathbf{B}_{\mathbf{diag}}$ estimated from MERRA2 using (5). (b) The anomaly correlation coefficients (ACC) for a linear prediction of the propagating model using the true $\mathbf{B}$ (yellow) and a linear prediction of the propagating model with the non-propagating $\mathbf{B}_{\mathbf{diag}}$ (purple). The colored labels on the x-axis represent the 10-folding timescales; on the y-axis, they represent the minimum value attained. The ranges represent bootstrapped 95% confidence intervals. The intervals are too narrow to be visible in panel (a). See Section 3.4 for details.

The greater available information translates to greater prediction skill (Figure 4b). Using each case's feedback matrix, we make 50,000 separate linear predictions of the propagating model's evolution. Each ensemble member has random initial conditions taken from a 500-year integration. The anomaly correlation coefficient captures the multidimensional correlation between the model and the prediction, and it shows that the non-propagating prediction has significantly worse skill at all lead times beyond one week. By the end of 4 weeks, the non-propagating prediction has about ¼ of the skill of the propagating prediction. While much of this reduced skill comes from an imperfect prediction system ($b_{12} \neq b_{21} \neq 0$), the propagating prediction still outperforms the non-propagating model predicting itself (Supplementary Figure 7b). Evidently, this idealized test does not identify the causes of underestimated predictability in GCMs. However, it demonstrates that propagation significantly impacts the NAO's predictability. Whether GCMs accurately simulate propagation is the subject of future work.

2. Discussion

We demonstrate that the NAO, previously synonymous with a stationary pattern of sea-level pressure (SLP) variance, is a quasi-periodic, propagating mode of variability for North Atlantic westerly wind, with implications for climate predictability, surface climate, and the response to human emissions. Like the SAM[52,66], the NAO propagates poleward with time, recurring every 145 days. This periodic signal appears in SLP and zonal wind anomalies, and it can be predicted with a simple model of eddy-mean flow interaction for the North Atlantic jet. Furthermore, the propagating NAO has coherent

climate impacts (temperature, precipitation, and SLP) which propagate poleward with the zonal wind anomalies.

The propagation of the NAO has several important consequences. One is that propagating jets respond to climate forcing in their jet-pulse modes (EOF2) and not only their jet-shift modes (EOF1)[40,63,68]. With this insight that the leading mode has a different spatial pattern (and timescale) than EOF1, the scientific community should revisit North Atlantic climate change studies which seek emergent constraints. Another consequence of propagation is that it increases the NAO's theoretical predictability. The quasi-semiannual nature of the propagation also confirms recent evidence of long-term NAO predictability[53,54].

An important caveat is that we have not resolved the signal-to-noise paradox which partially motivated this work. However, based on our predictability analysis, biases in GCM representation of NAO propagation should reduce models' prediction skill. Insomuch as underestimated midlatitude persistence contributes to the paradox[29], biases in NAO propagation would also contribute.

Additionally, our predictability analysis remains theoretical, based on a simple stochastic model of the NAO. The impacts of propagation on more complex forecast models are crucial to understand, but such experiments are beyond our current scope. Instead, using our simple model, we develop an intuition for the propagation–predictability nexus to guide future experimentation in more complex models.

An open question regarding propagating modes of variability is whether they might be influenced by human-caused climate change. We do not know if climate forcing will affect the speed or strength of propagating modes, which could have

important consequences for the persistence of the NAO[51]. Neither do we know how propagating modes of variability affect climate extremes, although the traditional NAO and the related Arctic Oscillation have been connected to such extremes[11,13,69].

The 145-day periodicity of the NAO's propagation also introduces the question of how propagation might affect predictability on subseasonal-to-seasonal timescales. The summertime NAO is influenced by the preceding wintertime NAO[12,70], and the semi-annual propagation described here could potentially link these seasons mechanistically. The scientific community should work to understand the deeper implications of propagation and its potential changes in a warmer climate.

3. Data and Methods

3.1. EOF Analysis

We define the NAO as the first two EOFs of vertically-integrated (850-100 hPa), longitudinal-mean (100°W–30°E), six-hourly zonal wind from 20°N–80°N, including the area-based weighting[56,66,71]. Prior to computing the EOFs, we deseasonalize the zonal wind data by subtracting the monthly climatology, we perform a linear detrending, and we remove ENSO through linear regression against the Multivariate ENSO Index version 2 (MEIv2)[72]. Prior to removal, data are downsampled to MEIv2 resolution (two-month running mean) before computing the regression slope, and then the ENSO-correlated wind is upsampled without interpolation (i.e., constant for each month) to match the 6-hourly frequency of the MERRA2 data.

The cross-EOF feedback parameters are computed following LH20 by regressing daily timeseries of EOF1 and EOF2 onto the projection timeseries for zonal wind and

the EMFC. The feedback parameters are computed over lag days 7-18 and averaged. To estimate the period and decay timescale, we reduce (5) to only the leading two EOFs, following LH20. $\mathcal{T}$, the period of propagation, is given by

$$\mathcal{T} = 4\pi\{[\tau_1^{-1} - \tau_2^{-1} - (b_{11} - b_{12})]^2 + 4b_{21}b_{12}\}^{-\frac{1}{2}}, \quad (6)$$

and σ, the inverse decay timescale, is given by

$$\sigma = -\frac{1}{2}(\tau_1^{-1} + \tau_2^{-1} - b_{11} - b_{22}). \quad (7)$$

where b_{ij} denote the elements of $\mathbf{B}$ and τ_i^{-1} the diagonal of $\mathbf{T^{-1}}$. See LH20 for details. Confidence intervals are "bootstrapped", meaning we randomly generate (with replacement) 1000 subsamples of length 30 years from the full data. We perform the analyses independently for each subsample and then use half the difference between the first and third quartiles of these subsamples to estimate their possible ranges.

The cross-EOF model also requires estimation of the frictional damping timescales $\tau_{\{1,2\}}$ to estimate the period and decay timescale of the coupled mode. This is done using the transfer function between the timeseries $\boldsymbol{m} \stackrel{\text{def}}{=} \mathbf{B}\boldsymbol{z} + \widetilde{\boldsymbol{m}}$ and $\boldsymbol{z}$ (see Lorenz and Hartmann[55], Appendix A). To compute the Fourier transforms, each timeseries is windowed (without padding) with an 8192-day Hann window with half-window overlap. For each window, we estimate the slope and intercept of the real and imaginary parts of the transfer function for periods longer than 30 days. This produces multiple estimates of both the slopes and intercepts which are averaged prior to computing τ. Uncertainty estimates for the timescales follow the bootstrapping procedure described above. Supplemental Figures 2 and 3 illustrate this procedure.

3.2. DMD Analysis

We utilize a nonlinear, data-driven approach, dynamic mode decomposition (DMD), to estimate the modes of $\mathbf{A}$. DMD works even if (3) cannot be represented as (1), because one can still find a linear embedding $\widetilde{\mathbf{A}}[\langle u \rangle]_{\Delta\lambda}$ for the nonlinear $\mathbf{A}([\langle u \rangle]_{\Delta\lambda})$ in an infinite-dimensional Hilbert space (though this is not the same as linearizing $\mathbf{A}$). After constructing a low-rank approximation of $\widetilde{\mathbf{A}}$ from the lag covariances in the data, a finite number of its eigenvectors can be estimated[73]. The detailed algorithm can be found in Tu et al.[74].

Before estimating the DMD modes, we deseasonalize and detrend the anomalies (with linear ENSO removal) as in Section 3.1. Also following EOF analysis, we weight the data by the square root of mass. We have two free parameters. One is the lag for computing the lag covariance matrix, and the other is the dimensionality to retain in the low-rank approximation of the dynamics. We perform the analysis over a range of lags (7-15 days) and dimensionalities which yield qualitatively similar results.

The final combination of parameters is chosen such that the leading mode is well-separated from the other modes. The criteria for separation are: 1) long decay timescales, 2) the pattern correlation between the DMD mode and the two leading EOFs, and 3) the spatial uniqueness of the leading mode. Following these criteria, we retain 90% of the variance (11 principal components) at a 10-day lag for the analysis in latitude-pressure space and 95% of the variance (8 principal components) at a 12-day lag for the vertically-averaged analysis used to estimate the DMD timeseries. See Supplemental Figure 8 for details.

For DMD modes, it is more complex to estimate a timeseries because dynamic modes $\mathbf{V}$ are not orthogonal since $\mathbf{A}$ is non-normal. In EOF-based analyses, one typically projects the mode linearly onto the original data to obtain the k-th mode's timeseries, $z_k(t) = \mathbf{v}_k^{\mathrm{T}}\mathbf{u}$. However, when modes are not orthogonal, we must approximate the adjoint operator $\mathbf{A}^\dagger$ († indicates conjugate transpose) from the eigenvectors of $\mathbf{A}$ as $\mathbf{A}^\dagger = (\mathbf{V}^\dagger)^{-1}\mathbf{\Lambda}\mathbf{V}^\dagger = \mathbf{Q}\mathbf{\Lambda}\mathbf{Q}^{-1}$, where the eigenvectors $\mathbf{Q}$ of $\mathbf{A}^\dagger$ are related to the original modes as $\mathbf{Q} = (\mathbf{V}^\dagger)^{-1}$. Because $\mathbf{V}$ is low rank, we use the right inverse of $\mathbf{V}^\dagger$, or $\mathbf{Q} = \mathbf{V}(\mathbf{V}^\dagger\mathbf{V})^{-1}$**,** extending Gallagher et al.[75] (Appendix A)**.** Thus, the k-th DMD timeseries is

$$z_k(t) = \mathbf{q}_k^\dagger\mathbf{u} = [(\mathbf{V}^\dagger\mathbf{V})^{-1}\mathbf{V}^\dagger\mathbf{u}]_k\,,$$

where $(\mathbf{X})_k$ indicates the k-th column of $\mathbf{X}$. The original $\mathbf{u}$ can be reconstructed, as in EOF analysis, as $\boldsymbol{u} = \sum_k \boldsymbol{v_k} z_k$.

Once obtained, we use the complex phase of the least-damped mode's timeseries to sort the deseasonalized, detrended, ENSO-removed anomalies (see Section 3.1) in surface temperature, pressure, and precipitation into 5° bins during October-March. We then average each bin. Anomalies are 15-day low-pass filtered before averaging. Robustness is indicated when at least 2/3 of the anomalies for each bin and latitude agree on the sign.

3.3. Spectral Analysis

To compute the power spectra of six-hourly zonal wind and daily SLP anomalies, we take the deseasonalized, detrended, ENSO-removed, North-Atlantic-mean anomalies (as in Section 3.1). To compute the power spectral density, each timeseries

is padded using the series reflected across its upper and lower boundaries, and it is windowed with a 4096-day Hann window with half-window overlap, resulting in 9 estimates of the Fourier transform, which are then squared, averaged, and normalized by the total variance. We fit the normalized spectrum at each latitude to a normalized discrete red noise spectrum[76], and we determine significance when peaks are above a certain multiple of this null spectrum. The multiplicative threshold is determined from the F-distribution, which is the null distribution for testing whether two different normal distributions with different degrees of freedom have different variances. Here, we estimate the spectrum has 2.4 degrees of freedom per estimate (21.6 in total) and the null spectrum has 1000 in total.

3.4. Predictability Analysis and Stochastic NAO Model

Given an idealized linear prediction system, we construct the "predictive information matrix" $\mathbf{G}(\tau) \stackrel{\text{def}}{=} \mathbf{C}(\tau)\mathbf{C}^{-1}(\infty)$**,** whose trace determines how the relative error grows with lead time τ[32,77]. In this framework, a prediction is "useful" at a given lead time when its error covariance is smaller than the climatological covariance. The singular values of $\mathbf{G}(\tau)$ are connected to information entropy, making them ideal predictability measures for a stochastic linear system[32,77], and they can be found using (2). We estimate the predictive information from $\mathbf{G}(\tau)$ following Tippett and Chang[32] as

$$\text{predictability} \stackrel{\text{def}}{=} 1 - \frac{\text{trace}\big(\mathbf{G}(\tau)\big)}{n} = \frac{1}{n}\sum_{k=1}^{n} \sigma_k^2 \left[\exp\left(\mathbf{C}^{-\frac{1}{2}}(\infty)\mathbf{A}\mathbf{C}^{\frac{1}{2}}(\infty)\right)\right] \qquad (8)$$

Where $\sigma_k[\mathbf{X}]$ indicates the k-th singular value of $\mathbf{X}$ and $n = 2$ is the rank of $\mathbf{A}$.

Inverting the climatological covariance matrix is non-trivial, as the high dimensionality and short length of the observational data make it ill-conditioned[32,40]. Thus, we develop a stochastically driven, reduced-order NAO model using (5), following both LH20 and Simpson et al.[56]. This model allows for long time integrations (500 years) with comparable statistics to the real NAO, enabling a better estimate for $\mathbf{C}^{-1}(\infty)$.

The stochastic model implements (5) for 2 EOFs, where $\mathbf{B}$ and $\mathbf{T}$ are estimated from the data (see Section 3.1) and modified as described in the text. $\widetilde{\boldsymbol{m}}$ is generated using two uncoupled, second-order autoregressive (AR-2) processes driven by white noise, $\widetilde{m}_i(t) = 0.6\,\widetilde{m}_i(t-1) - 0.3\,\widetilde{m}_i(t-2) + \tilde{\varepsilon}$, with the coefficients following previous studies[51,56], and where $\tilde{\varepsilon}(-1{,}1)$ is a white noise distribution between -1 and 1. The model is integrated using the implicit trapezoidal technique for stability.

Linear predictions of the stochastic model are $\mathbf{z_0}e^{\mathbf{A}\tau}$, where $\mathbf{z_0}$ are the random initial conditions drawn from the 500-year integration. The skill is measured by the anomaly correlation coefficient (ACC), the Pearson product-moment correlation between the predicted vector and the model output for each of the 50,000 ensemble members. 95% confidence intervals are bootstrapped using 2000 estimates of the ACC with a random subset of 10,000 of the ensemble members (with replacement). This strategy is repeated for estimating 95% confidence intervals of the predictability (8).

3.5. Data Sources

Data for this work were obtained from the NASA MERRA2 reanalysis[78], which are gridded at approximately 0.5° latitude by 0.625° longitude resolution, with 29 vertical levels between surface and mid-stratosphere (30hPa). Six-hourly horizontal velocity and

surface climate data were downloaded for 1980-2023. These high-frequency data are needed to resolve medium-scale waves[39].

Sea-surface temperature data from 1982-2023 were downloaded from the NOAA OISST dataset[79] with approximately 0.25°×0.25° horizontal resolution. The start year of 1982 is the first full year of OISST data available. OISST data were selected because MERRA2 assimilates this data during most of the relevant years[78]. MEIv2 timeseries data are publicly available from NOAA[72].

Acknowledgements

SS would like to acknowledge Noboru Nakamura for funding support and computational resources supporting this work. We acknowledge the Python libraries Numpy, SciPy, Xarray, and Matplotlib. SS was funded through NSF Award 2154523, PI Noboru Nakamura. PS was funded through NSF Grant 1813981. JL was supported both by the U.S. DOE Office of Science - Biological and Environmental Research as part of the Regional and Global Modeling and Analysis Program and by startup projects 3001000-862401013230 and 3001000-862505020010 at Ocean University of China.

Data Availability

MERRA2, OISST, and MEIv2 data used for this analysis are publicly available from their respective sources (see Section 3.5).

Code Availability

Analysis code is available from the corresponding author upon request.

References

1. Wallace, J. M., & Gutzler, D. S. (1981). Teleconnections in the Geopotential Height Field during the Northern Hemisphere Winter. *Monthly Weather Review*, *109*(4), 784–812. https://doi.org/10.1175/1520-0493(1981)109<0784:TITGHF>2.0.CO;2
2. Greatbatch, R. J. (2000). The North Atlantic Oscillation. *Stochastic Environmental Research and Risk Assessment*, *14*(4), 213–242. https://doi.org/10.1007/s004770000047
3. Hurrell, J. W., Kushnir, Y., Ottersen, G., & Visbeck, M. (2003). An overview of the North Atlantic Oscillation. *Geophysical Monograph Series* (Vol. 134, pp. 1–35). https://doi.org/10.1029/134GM01
4. Vallis, G. K., Gerber, E. P., Kushner, P. J., & Cash, B. A. (2004). A Mechanism and Simple Dynamical Model of the North Atlantic Oscillation and Annular Modes. *Journal of the Atmospheric Sciences*, 61(3), 264–280. https://doi.org/10.1175/1520-0469(2004)061<0264:AMASDM>2.0.CO;2
5. Walker, G. T. (1924). Correlation in seasonal variation of weather. IX. A further study of world weather. *Memoirs India Meteorol Dep*, *24*, 275–333.
6. Deser, C., Alexander, M. A., Xie, S.-P., & Phillips, A. S. (2009). Sea Surface Temperature Variability: Patterns and Mechanisms. *Annual Review of Marine Science*, 2(1), 115–143. https://doi.org/10.1146/annurev-marine-120408-151453
7. Scaife, A. A., Arribas, A., Blockley, E., Brookshaw, A., Clark, R. T., Dunstone, N., et al. (2014). Skillful long-range prediction of European and North American

winters. *Geophysical Research Letters*, *41*(7), 2514–2519. https://doi.org/10.1002/2014GL059637

8. Clement, A., Bellomo, K., Murphy, L. N., Cane, M. A., Mauritsen, T., Rädel, G., & Stevens, B. (2015). The Atlantic Multidecadal Oscillation without a role for ocean circulation. *Science*, *350*(6258), 320–324. https://doi.org/10.1126/science.aab3980
9. Delworth, T. L., Zeng, F., Vecchi, G. A., Yang, X., Zhang, L., & Zhang, R. (2016). The North Atlantic Oscillation as a driver of rapid climate change in the Northern Hemisphere. *Nature Geoscience*, *9*(7), 509–512. https://doi.org/10.1038/ngeo2738
10. Wettstein, J. J., & Mearns, L. O. (2002). The Influence of the North Atlantic–Arctic Oscillation on Mean, Variance, and Extremes of Temperature in the Northeastern United States and Canada. *Journal of Climate*, *15*(24), 3586–3600. https://doi.org/10.1175/1520-0442(2002)015<3586:TIOTNA>2.0.CO;2
11. Scaife, Adam A., Folland, C. K., Alexander, L. V., Moberg, A., & Knight, J. R. (2008). European Climate Extremes and the North Atlantic Oscillation. *Journal of Climate*, *21*(1), 72–83. https://doi.org/10.1175/2007JCLI1631.1
12. Otomi, Y., Tachibana, Y., & Nakamura, T. (2013). A possible cause of the AO polarity reversal from winter to summer in 2010 and its relation to hemispheric extreme summer weather. *Climate Dynamics*, 40(7), 1939–1947. https://doi.org/10.1007/s00382-012-1386-0
13. Zanardo, S., Nicotina, L., Hilberts, A. G. J., & Jewson, S. P. (2019). Modulation of Economic Losses from European Floods by the North Atlantic Oscillation.

Geophysical Research Letters, 46(5), 2563–2572. https://doi.org/10.1029/2019GL081956

14. Bracegirdle, T. J., Lu, H., Eade, R., & Woollings, T. (2018). Do CMIP5 Models Reproduce Observed Low-Frequency North Atlantic Jet Variability? *Geophysical Research Letters*, 45(14), 7204–7212. https://doi.org/10.1029/2018GL078965
15. D. Smith, et al. (2020). *North Atlantic climate far more predictable than models imply*. *Nature*, 583(7818), 796–800. https://doi.org/10.1038/s41586-020-2525-0
16. Hamouda, M. E., Pasquero, C., & Tziperman, E. (2021). Decoupling of the Arctic Oscillation and North Atlantic Oscillation in a warmer climate. *Nature Climate Change*, *11*(2), 137–142. https://doi.org/10.1038/s41558-020-00966-8
17. Eade, R., Stephenson, D. B., Scaife, A. A., & Smith, D. M. (2022). Quantifying the rarity of extreme multi-decadal trends: how unusual was the late twentieth century trend in the North Atlantic Oscillation? *Climate Dynamics*, *58*(5), 1555–1568. https://doi.org/10.1007/s00382-021-05978-4
18. Kuzmina, S. I., Bengtsson, L., Johannessen, O. M., Drange, H., Bobylev, L. P., & Miles, M. W. (2005). The North Atlantic Oscillation and greenhouse-gas forcing. *Geophysical Research Letters*, *32*(4). https://doi.org/10.1029/2004GL021064
19. Gillett, N. P., & Fyfe, J. C. (2013). Annular mode changes in the CMIP5 simulations. *Geophysical Research Letters*, *40*(6), 1189–1193. https://doi.org/10.1002/grl.50249
20. Christiansen, B., Yang, S., & Matte, D. (2022). The Forced Response and Decadal Predictability of the North Atlantic Oscillation: Nonstationary and Fragile

Skills. *Journal of Climate*, *35*(18), 5869–5882. https://doi.org/10.1175/JCLI-D-21-0807.1

21. Blackport, R., & Fyfe, J. C. (2022). Climate models fail to capture strengthening wintertime North Atlantic jet and impacts on Europe. *Science Advances*, *8*(45). https://doi.org/10.1126/sciadv.abn3112
22. Eade, R., Smith, D., Scaife, A., Wallace, E., Dunstone, N., Hermanson, L., & Robinson, N. (2014). Do seasonal-to-decadal climate predictions underestimate the predictability of the real world? *Geophysical Research Letters*, *41*(15), 5620–5628. https://doi.org/10.1002/2014GL061146
23. Scaife, A. A., & Smith, D. (2018). A signal-to-noise paradox in climate science. *Npj Climate and Atmospheric Science*, *1*(1), 1–8. https://doi.org/10.1038/s41612-018-0038-4
24. Brener, D. J. (2024). A hypothesis on ergodicity and the signal-to-noise paradox. Atmospheric Science Letters, 25(11), e1265. https://doi.org/10.1002/asl.1265
25. Strommen, K., & Palmer, T. N. (2019). Signal and noise in regime systems. *Quarterly Journal of the Royal Meteorological Society*, 145(718), 147–163. https://doi.org/10.1002/qj.3414
26. Strommen, K., MacRae, M., & Christensen, H. (2023). On the Relationship Between Reliability Diagrams and the “Signal-To-Noise Paradox.” *Geophysical Research Letters*, *50*(14), e2023GL103710. https://doi.org/10.1029/2023GL103710

27. Zhang, W., & Kirtman, B. (2019). Understanding the Signal-to-Noise Paradox with a Simple Markov Model. *Geophysical Research Letters*, 46(22), 13308–13317. https://doi.org/10.1029/2019GL085159

28. Hardiman, S. C., Dunstone, N. J., Scaife, A. A., Smith, D. M., Comer, R., Nie, Y., & Ren, H.-L. (2022). Missing eddy feedback may explain weak signal-to-noise ratios in climate predictions. *Npj Climate and Atmospheric Science*, *5*(1), 1–8. https://doi.org/10.1038/s41612-022-00280-4

29. Garfinkel, C. I., Knight, J., Taguchi, M., Schwartz, C., Cohen, J., Chen, W., et al. (2024). Development of the signal-to-noise paradox in subseasonal forecasting models: When? Where? Why? *Quarterly Journal of the Royal Meteorological Society*, *150*(764), 4417–4436. https://doi.org/10.1002/qj.4822

30. Hasselmann, K. (1976). Stochastic climate models Part I. Theory. *Tellus*, *28*(6), 473–485. https://doi.org/10.1111/j.2153-3490.1976.tb00696.x

31. Ring, M. J., & Plumb, R. A. (2008). The Response of a Simplified GCM to Axisymmetric Forcings: Applicability of the Fluctuation–Dissipation Theorem. *Journal of the Atmospheric Sciences*, *65*(12), 3880–3898. https://doi.org/10.1175/2008JAS2773.1

32. Tippett, M. K., & Chang, P. (2003). Some theoretical considerations on predictability of linear stochastic dynamics. *Tellus A*, *55*(2), 148–157. https://doi.org/10.1034/j.1600-0870.2003.00008.x

33. Penland, C. (1989). Random Forcing and Forecasting Using Principal Oscillation Pattern Analysis. *Monthly Weather Review*, *117*(10), 2165–2185. https://doi.org/10.1175/1520-0493(1989)117<2165:RFAFUP>2.0.CO;2

34. Leith, C. E. (1975). Climate Response and Fluctuation Dissipation. *Journal of the Atmospheric Sciences*, *32*(10), 2022–2026. https://doi.org/10.1175/1520-0469(1975)032<2022:CRAFD>2.0.CO;2

35. Gritsun, A., & Branstator, G. (2007). Climate Response Using a Three-Dimensional Operator Based on the Fluctuation–Dissipation Theorem. *Journal of the Atmospheric Sciences*, *64*(7), 2558–2575. https://doi.org/10.1175/JAS3943.1

36. Lutsko, N. J., Held, I. M., & Zurita-Gotor, P. (2015). Applying the Fluctuation–Dissipation Theorem to a Two-Layer Model of Quasigeostrophic Turbulence. *Journal of the Atmospheric Sciences*, *72*(8), 3161–3177. https://doi.org/10.1175/JAS-D-14-0356.1

37. Hassanzadeh, P., & Kuang, Z. (2016). The Linear Response Function of an Idealized Atmosphere. Part II: Implications for the Practical Use of the Fluctuation–Dissipation Theorem and the Role of Operator's Nonnormality. *Journal of the Atmospheric Sciences*, *73*(9), 3441–3452. https://doi.org/10.1175/JAS-D-16-0099.1

38. Simpson, I. R., & Polvani, L. M. (2016). Revisiting the relationship between jet position, forced response, and annular mode variability in the southern midlatitudes. *Geophysical Research Letters*, *43*(6), 2896–2903. https://doi.org/10.1002/2016GL067989

39. Ma, D., Hassanzadeh, P., & Kuang, Z. (2017). Quantifying the Eddy–Jet Feedback Strength of the Annular Mode in an Idealized GCM and Reanalysis Data. *Journal of the Atmospheric Sciences*, *74*(2), 393–407. https://doi.org/10.1175/JAS-D-16-0157.1

40. Sheshadri, A., & Plumb, R. A. (2017). Propagating Annular Modes: Empirical Orthogonal Functions, Principal Oscillation Patterns, and Time Scales. *Journal of the Atmospheric Sciences*, *74*(5), 1345–1361. https://doi.org/10.1175/JAS-D-16-0291.1

41. Albers, J. R., & Newman, M. (2021). Subseasonal predictability of the North Atlantic Oscillation. *Environmental Research Letters*, *16*(4), 044024. https://doi.org/10.1088/1748-9326/abe781

42. Gerber, E. P., Polvani, L. M., & Ancukiewicz, D. (2008). Annular mode time scales in the Intergovernmental Panel on Climate Change Fourth Assessment Report models. *Geophysical Research Letters*, *35*(22). https://doi.org/10.1029/2008GL035712

43. Simpson, I. R., Bacmeister, J., Neale, R. B., Hannay, C., Gettelman, A., Garcia, R. R., et al. (2020). An Evaluation of the Large-Scale Atmospheric Circulation and Its Variability in CESM2 and Other CMIP Models. *Journal of Geophysical Research: Atmospheres*, *125*(13), e2020JD032835. https://doi.org/10.1029/2020JD032835

44. Feldstein, S. B., & Franzke, C. (2006). Are the North Atlantic Oscillation and the Northern Annular Mode distinguishable? *Journal of the Atmospheric Sciences*, 63(12), 2915–2930. https://doi.org/10.1175/JAS3798

45. Barnes, E. A., & Hartmann, D. L. (2010). Dynamical Feedbacks and the Persistence of the NAO. *Journal of the Atmospheric Sciences*, *67*(3), 851–865. https://doi.org/10.1175/2009JAS3193.1

46. Hasselmann, K. (1988). PIPs and POPs: The reduction of complex dynamical systems using principal interaction and oscillation patterns. *Journal of Geophysical Research: Atmospheres*, 93(D9), 11015–11021. https://doi.org/10.1029/JD093iD09p11015

47. Fyfe, J. C., & Lorenz, D. J. (2005). Characterizing Midlatitude Jet Variability: Lessons from a Simple GCM. *Journal of Climate*, 18(16), 3400–3404. https://doi.org/10.1175/JCLI3486.1

48. Monahan, A. H., & Fyfe, J. C. (2006). On the Nature of Zonal Jet EOFs. *Journal of Climate*, 19(24), 6409–6424. https://doi.org/10.1175/JCLI3960.1

49. Monahan, A. H., Fyfe, J. C., Ambaum, M. H. P., Stephenson, D. B., & North, G. R. (2009). Empirical Orthogonal Functions: The Medium is the Message. *Journal of Climate*, 22(24), 6501–6514. https://doi.org/10.1175/2009JCLI3062.1

50. Gerber, E. P., & Thompson, D. W. J. (2017). What Makes an Annular Mode "Annular"? *Journal of the Atmospheric Sciences*, *74*(2), 317–332. https://doi.org/10.1175/JAS-D-16-0191.1

51. Lubis, S. W., & Hassanzadeh, P. (2020). An Eddy–Zonal Flow Feedback Model for Propagating Annular Modes. *Journal of the Atmospheric Sciences*, *78*(1), 249–267. https://doi.org/10.1175/JAS-D-20-0214.1

52. Lubis, S. W., & Hassanzadeh, P. (2023). The Intrinsic 150-Day Periodicity of the Southern Hemisphere Extratropical Large-Scale Atmospheric Circulation. *AGU Advances*, *4*(3), e2022AV000833. https://doi.org/10.1029/2022AV000833

53. Scaife, A. A., Hermanson, L., van Niekerk, A., Andrews, M., Baldwin, M. P., Belcher, S., et al. (2022). Long-range predictability of extratropical climate and

the length of day. *Nature Geoscience*, *15*(10), 789–793. https://doi.org/10.1038/s41561-022-01037-7

54. Scaife, Adam A., Dunstone, N., Hardiman, S., Ineson, S., Li, C., Lu, R., et al. (2024). ENSO affects the North Atlantic Oscillation 1 year later. *Science*. https://doi.org/10.1126/science.adk4671

55. Lorenz, D. J., & Hartmann, D. L. (2001). Eddy–Zonal Flow Feedback in the Southern Hemisphere. *Journal of the Atmospheric Sciences*, *58*(21), 3312–3327. https://doi.org/10.1175/1520-0469(2001)058<3312:EZFFIT>2.0.CO;2

56. Simpson, I. R., Shepherd, T. G., Hitchcock, P., & Scinocca, J. F. (2013). Southern Annular Mode Dynamics in Observations and Models. Part II: Eddy Feedbacks. *Journal of Climate*, *26*(14), 5220–5241. https://doi.org/10.1175/JCLI-D-12-00495.1

57. Lorenz, D. J., & Hartmann, D. L. (2003). Eddy–Zonal Flow Feedback in the Northern Hemisphere Winter. *Journal of Climate*, *16*(8), 1212–1227. https://doi.org/10.1175/1520-0442(2003)16<1212:EFFITN>2.0.CO;2

58. Lu, J., Harrop, B. E., Lubis, S. W., Smith, S., Chen, G., & Leung, L. R. (2024). The Role of Cloud Radiative Effects in the Propagating Southern Annular Mode. *Journal of Geophysical Research: Atmospheres*, *129*(8), e2023JD040428. https://doi.org/10.1029/2023JD040428

59. Schmid, P. J. (2022). Dynamic Mode Decomposition and Its Variants. *Annual Review of Fluid Mechanics*, *54*(Volume 54, 2022), 225–254. https://doi.org/10.1146/annurev-fluid-030121-015835

60. Lee, S., Son, S.-W., Grise, K., & Feldstein, S. B. (2007). A Mechanism for the Poleward Propagation of Zonal Mean Flow Anomalies. *Journal of the Atmospheric Sciences*, *64*(3), 849–868. https://doi.org/10.1175/JAS3861.1

61. Riehl, H., Yeh, T. C., & Seur, N. E. L. (1950). A STUDY OF VARIATIONS OF THE GENERAL CIRCULATION. *Journal of the Atmospheric Sciences*, *7*(3), 181–194. https://doi.org/10.1175/1520-0469(1950)007<0181:ASOVOT>2.0.CO;2

62. Feldstein, S. B. (1998). An Observational Study of the Intraseasonal Poleward Propagation of Zonal Mean Flow Anomalies. *Journal of the Atmospheric Sciences*, *55*(15), 2516–2529. https://doi.org/10.1175/1520-0469(1998)055<2516:AOSOTI>2.0.CO;2

63. Lorenz, D. J. (2023). A Simple Mechanistic Model of Wave–Mean Flow Feedbacks, Poleward Jet Shifts, and the Annular Mode. *Journal of the Atmospheric Sciences*, *80*(2), 549–568. https://doi.org/10.1175/JAS-D-22-0056.1

64. Thompson, D. W. J., & Wallace, J. M. (2000). Annular Modes in the Extratropical Circulation. Part I: Month-to-Month Variability. *Journal of Climate*, *13*(5), 1000–1016. https://doi.org/10.1175/1520-0442(2000)013<1000:AMITEC>2.0.CO;2

65. de Viron, O., & Dickey, J. O. (2014). The two types of El-Niño and their impacts on the length of day. *Geophysical Research Letters*, *41*(10), 3407–3412. https://doi.org/10.1002/2014GL059948

66. Smith, S., Lu, J., & Staten, P. W. (2024). Diabatic Eddy Forcing Increases Persistence and Opposes Propagation of the Southern Annular Mode in MERRA-2. *Journal of the Atmospheric Sciences*, *81*(4), 743–764. https://doi.org/10.1175/JAS-D-23-0019.1

679 67. Tziperman, E., Stone, L., Cane, M. A., & Jarosh, H. (1994). El Niño Chaos:
680 Overlapping of Resonances Between the Seasonal Cycle and the Pacific Ocean-
681 Atmosphere Oscillator. *Science*, *264*(5155), 72–74.
682 https://doi.org/10.1126/science.264.5155.72
683 68. Son, S.-W., & Lee, S. (2006). Preferred Modes of Variability and Their
684 Relationship with Climate Change. *Journal of Climate*, *19*(10), 2063–2075.
685 https://doi.org/10.1175/JCLI3705.1
686 69. Chen, G., Lu, J., Burrows, D. A., & Leung, L. R. (2015). Local finite-amplitude
687 wave activity as an objective diagnostic of midlatitude extreme weather.
688 *Geophysical Research Letters*, *42*(24), 10,952-10,960.
689 https://doi.org/10.1002/2015GL066959
690 70. Ogi, M., Yamazaki, K., & Tachibana, Y. (2004). The summertime annular mode
691 in the Northern Hemisphere and its linkage to the winter mode. *Journal of*
692 *Geophysical Research: Atmospheres*, *109*(D20).
693 https://doi.org/10.1029/2004JD004514
694 71. Baldwin, M. P., Stephenson, D. B., & Jolliffe, I. T. (2009). Spatial Weighting and
695 Iterative Projection Methods for EOFs. *Journal of Climate*, *22*(2), 234–243.
696 https://doi.org/10.1175/2008JCLI2147.1
697 72. Zhang, T., Hoell, A., Perlwitz, J., Eischeid, J., Murray, D., Hoerling, M., & Hamill,
698 T. M. (2019). Towards Probabilistic Multivariate ENSO Monitoring. *Geophysical*
699 *Research Letters*, *46*(17–18), 10532–10540.
700 https://doi.org/10.1029/2019GL083946

73. Rowley, C. W., Mezić, I., Bagheri, S., Schlatter, P., & Henningson, D. S. (2009). Spectral analysis of nonlinear flows. *Journal of Fluid Mechanics*, *641*, 115–127. https://doi.org/10.1017/S0022112009992059

74. Tu, J. H., Rowley, C. W., Luchtenburg, D. M., Brunton, S. L., & Kutz, J. N. (2014). On dynamic mode decomposition: Theory and applications. *Journal of Computational Dynamics*, *1*(2), 391–421. https://doi.org/10.3934/jcd.2014.1.391

75. Gallagher, F., von Storch, H., Schnur, R., & Hannoschöck, G. (1991). The POP Manual. https://doi.org/10.2312/WDCC/DKRZ_REPORT_NO01

76. Gilman, D. L., Fuglister, F. J., & Mitchell, J. M. (1963). On the Power Spectrum of "Red Noise." *Journal of the Atmospheric Sciences*, *20*(2), 182–184. https://doi.org/10.1175/1520-0469(1963)020<0182:OTPSON>2.0.CO;2

77. Schneider, T., & Griffies, S. M. (1999). A Conceptual Framework for Predictability Studies. *Journal of Climate*, *12*(10), 3133–3155. https://doi.org/10.1175/1520-0442(1999)012<3133:ACFFPS>2.0.CO;2

78. Gelaro, R., McCarty, W., Suárez, M. J., Todling, R., Molod, A., Takacs, L., et al. (2017). The Modern-Era Retrospective Analysis for Research and Applications, Version 2 (MERRA-2). *Journal of Climate*, *30*(14), 5419–5454. https://doi.org/10.1175/JCLI-D-16-0758.1

79. Huang, B., Liu, C., Banzon, V., Freeman, E., Graham, G., Hankins, B., et al. (2021). Improvements of the Daily Optimum Interpolation Sea Surface Temperature (DOISST) Version 2.1. *Journal of Climate*, *34*(8), 2923–2939. https://doi.org/10.1175/JCLI-D-20-0166.1

Supplemental Materials for "The Subseasonal North Atlantic Oscillation is a Quasi-Semiannual, Propagating Disturbance"

Samuel Smith[1*], Jian Lu[2,3], and Paul W. Staten[4]

[1]Dept. of Geophysical Sciences, University of Chicago, Chicago, IL 60615

[2]Coll. of Oceanic and Atmospheric Sciences, Ocean University of China, Qingdao, China 266100

[3]Earth Sciences Division, Pacific Northwest National Laboratory, Richland, WA 99354

[4]Dept. of Earth and Atmospheric Sciences, Indiana University, Bloomington, IN 47405

*5734 S. Ellis Ave, Chicago, IL 60637; samuelsmith@uchicago.edu

1. Derivation of Regional Momentum Budget

We begin from the quasi-geostrophic, free-tropospheric-mean $\langle \cdot \rangle$, sectoral-average $[\cdot]_{\Delta\lambda}$, momentum budget. Unlike in the hemispheric zonal-mean, we must account for the zonal advection of momentum and the ageostrophic Coriolis torque:

$$\frac{\partial [\langle u \rangle]_{\Delta\lambda}}{\partial t} + \frac{\partial [\langle v'u' \rangle \cos^2 \phi]_{\Delta\lambda}}{(a \cos^2 \phi)\, \partial \phi} = -\left[\frac{\partial \langle \Phi + u^2 \rangle}{(a \cos\theta)\, \partial \lambda}\right]_{\Delta\lambda} + f[\langle v \rangle]_{\Delta\lambda} + [X_s]_{\Delta\lambda}. \qquad \text{(S1)}$$

Here u and v are zonal and meridional momentum, respectively, Φ represents geopotential height, f is the Coriolis parameter, X_s is surface friction, λ and ϕ are longitude and latitude, respectively, a is the Earth's radius, and primes represent deviations from the hemispheric zonal mean (not the regional mean).

When the timescales are sufficiently short and the zonal length scale is much longer than the meridional length scale of the eddy-producing region, waves within the region satisfy the WKB approximation and the effect on the one boundary cancels with that upon the other (Vallis et al. 2004). Thus, the first two terms on the rhs of (S1) are negligible (the second term vanishes due to continuity with WKB, which implies $[\langle v \rangle]_{\Delta\lambda} \to 0$ as $\Delta\lambda \to 360$), and (S1) becomes (3):

$$\partial_t [\langle u \rangle]_{\Delta\lambda} \approx [\langle M \rangle]_{\Delta\lambda} + [X_s]_{\Delta\lambda}\,.$$

Here, we defined the eddy momentum flux convergence $M \stackrel{\text{def}}{=} -\frac{\partial (v'u' \cos^2 \phi)}{(a \cos^2 \phi)\, \partial \phi}$.

2. Assessment of the Linear Model (5)

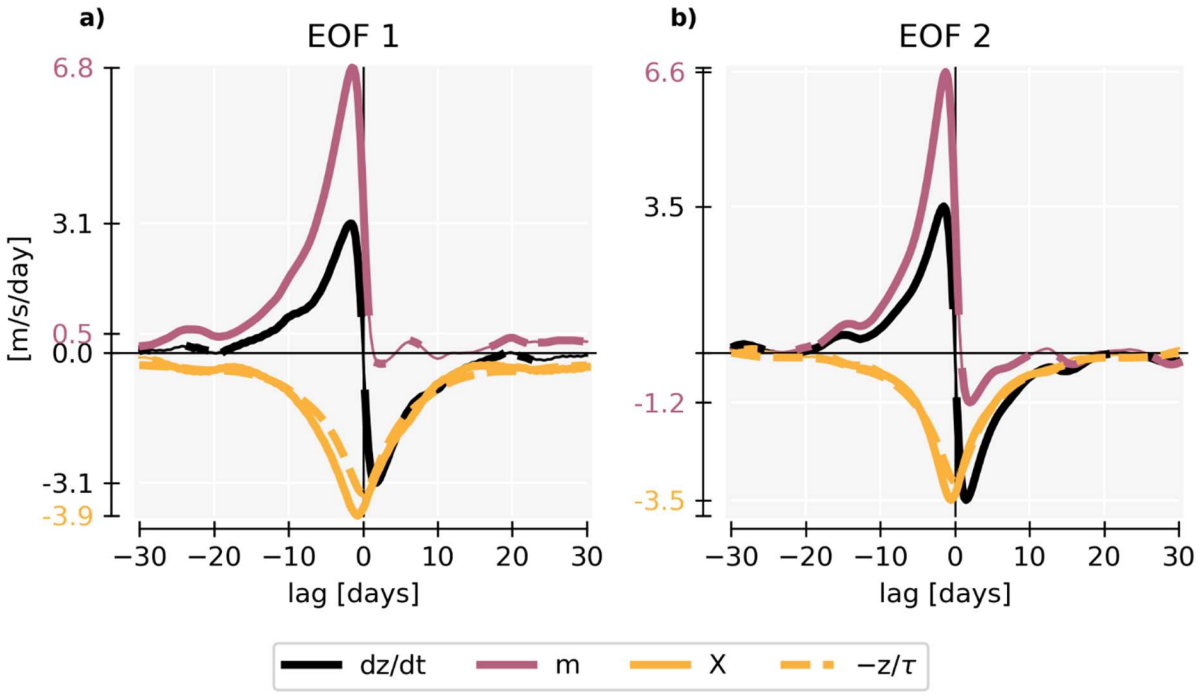

Figure S1: The EOF1 (a) and EOF2 (b) momentum budgets for the North-Atlantic-mean, vertically integrated (850-100 hPa) zonal wind in MERRA2 from 1980-2023, representing the first two EOFs for (5). All EOF1 terms (a) are regressed against the EOF1 index, and similarly for EOF2 (b). The blue lines $\left(\frac{dz}{dt}\right)$ represent the lag correlations for each index with the EOF1- and EOF2-projected zonal wind tendencies. m is the EOF-projected eddy momentum flux convergence (EMFC). X is the (EOF-projected) residual between the zonal wind tendency and EMFC (solid brown), compared to linear Rayleigh damping (dashed brown). Lines appear thin where the 90% confidence intervals contain zero.

Figure S1 shows the terms in (5), regressed against the index itself ($\boldsymbol{z}$). $\boldsymbol{m} \overset{\text{def}}{=} \mathbf{B}\boldsymbol{z} + \tilde{\boldsymbol{m}}$ combines the linear and stochastic parts. X is computed residually as $\partial_t[\langle u\rangle]_{\boldsymbol{\Delta\lambda}} - [\langle M\rangle]_{\boldsymbol{\Delta\lambda}}$ before projecting it onto the EOFs. $-\mathbf{T}^{-1}\boldsymbol{z}$ represents Rayleigh friction for each mode, with the timescales τ_{ii} estimated as in Section 3.1 (more detail below). The Rayleigh friction and the residual agree strongly, and, because WKB theory suggests the other terms in (S1) should be small, this agreement confirms that the residual is essentially friction which can be modeled as Rayleigh damping. This confirms that boundary effects are negligible.

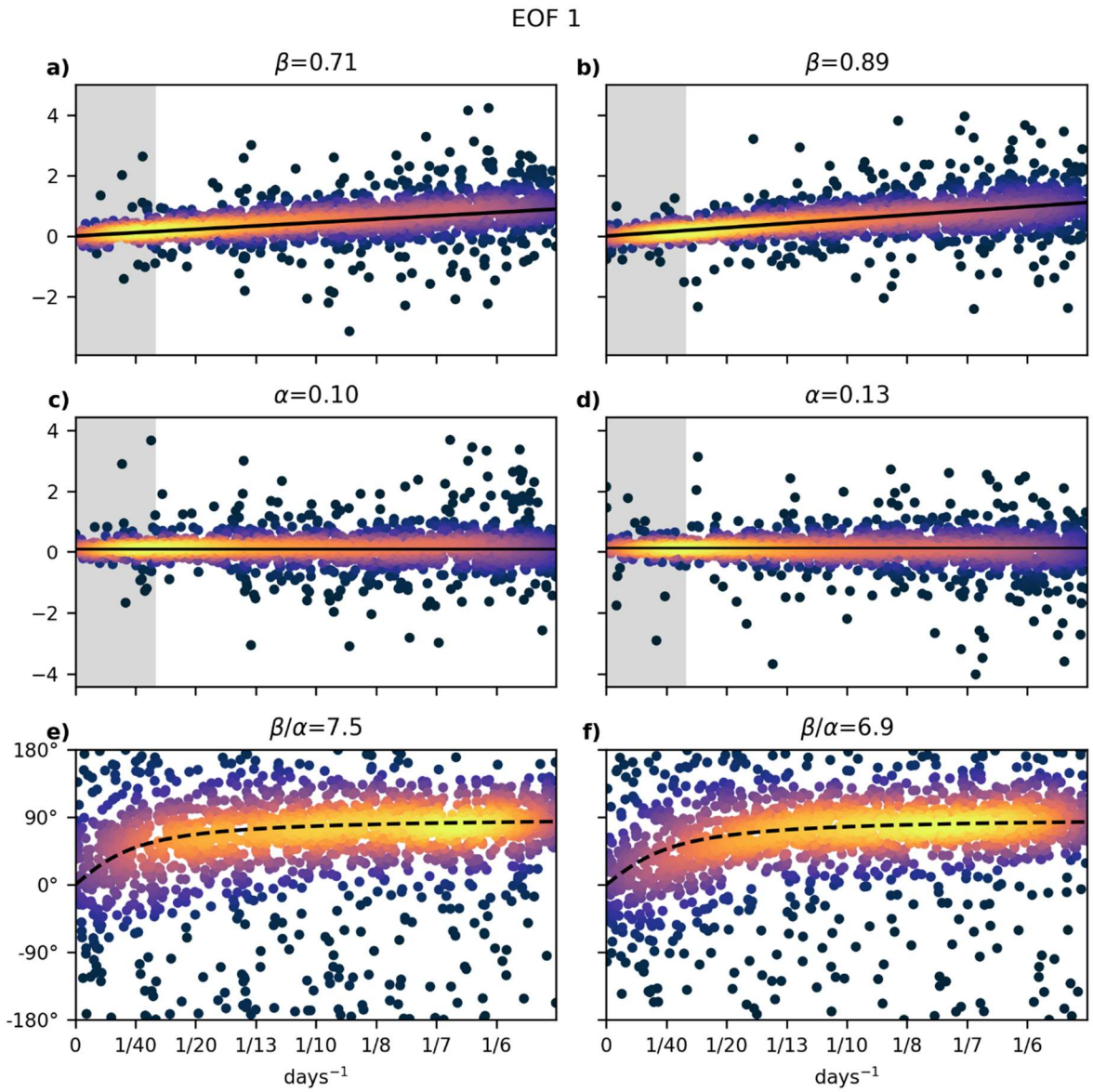

Figure S2: Imaginary (a,b) and real (c,d) parts of the transfer function used to estimate the frictional damping timescale for EOF1 (see Section 3.1, and Lorenz and Hartmann 2001, their Figure 3). Coloring shows the kernel density estimate of the number of points. Black line shows the estimated linear fit. The phase difference between m and z as a function of frequency ω is shown in (e,f), along with the predicted phase difference ($\arctan(\omega\tau)$, black, dashed line) for a system obeying (5) . The regression is performed for two, windowed, overlapping sections of the daily 1980-2023 timeseries. Only the low-frequency (less than 30 days; indicated by the gray shaded region in a-d) portion of the transfer function is fit.

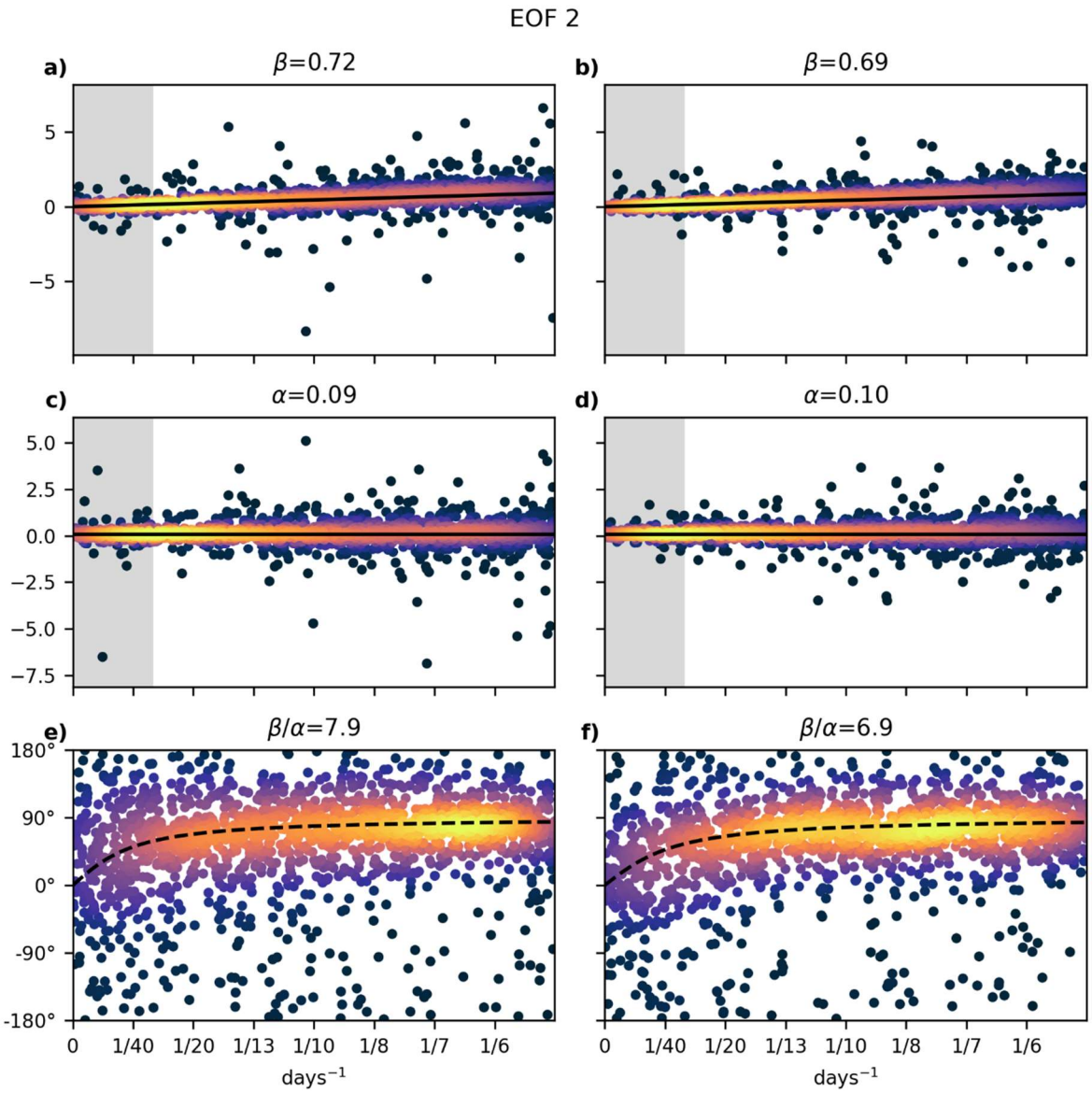

Figure S3: As in Figure S2, but for EOF2.

Figures S2 and S3 display the imaginary (a,b) and real (c,d) parts of the transfer function for $\boldsymbol{m} \stackrel{\text{def}}{=} \mathbf{B}\boldsymbol{z} + \tilde{\boldsymbol{m}}$ and $\boldsymbol{z}$ for both overlapping windows used for the Fourier transform (see Section 3.1). If (5) applies, then the transfer function should follow $\frac{M^*Z}{Z^*Z} = \tau^{-1} + i\omega$, where uppercase letters denote the respective Fourier transforms. Following Lorenz and Hartmann (2001, Appendix A), we restrict the domain to low-frequencies (gray shading) and fit the real part as a constant α and the imaginary part as a zero-intercept regression with slope β. We average over both estimates before computing $\tau = \beta/\alpha$. For validation, we compare the phase difference between m and z to the phase difference implied by (5), $\arctan(\omega\tau)$. The fit suggests the validity of (5).

3. *Propagation in EOF Space*

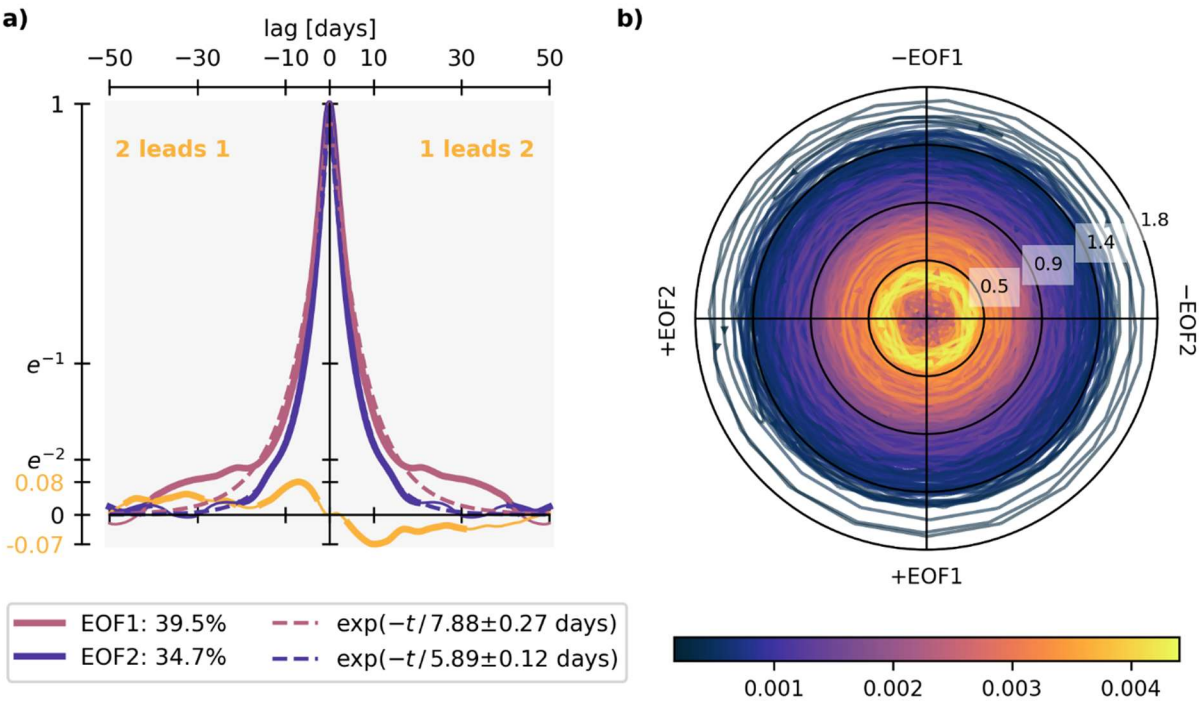

Figure S4: (a) Autocorrelations of EOF1 and EOF2 of vertically integrated, North-Atlantic-mean (100°W–30°E) zonal wind and their cross-regression in MERRA2 from 1980-2023 (solid lines). An exponential fit to EOF1 and 2 autocorrelations, with timescales in the legend (dashed lines). The fraction of variance explained by each EOF is shown in the legend. Lines appear thin where the bootstrapped 90% confidence interval contains zero. (b) Complex EOF phase-space trajectories of low-frequency (40-day) poleward propagation events. The complex timeseries utilizes the same data as (a). The color of the lines is proportional to the density of the trajectories estimated by kernel density estimation. Arrows show the direction from one timestep to the next; counter-clockwise represents poleward propagation.

Figure S4a shows the autocorrelations and cross-correlations for the first two EOFs of North Atlantic, free-tropospheric zonal wind, computed as detailed in Section 3.1. Propagating annular modes have three hallmarks in EOF-space (Sheshadri and Plumb 2017), which are all present for the NAO: 1) the fraction of variance explained in EOF2 (34.7%) is more than half the variance explained by EOF1 $\left(39.5\% \times \frac{1}{2} = 19.8\%\right)$, 2) the decorrelation timescale (estimated by curve-fitting to an exponential function) is similar (7.9 days versus 5.9 days), and 3) non-zero cross-correlations at non-zero lags.

Because the cross-correlations are weak [likely because the NAO can propagate both equatorward and poleward (Lorenz 2023)], we also examine trajectories of the timeseries $-\text{EOF2} - i\,\text{EOF1}$, which has the same phase as the DMD timeseries, in

Figure S4b. To compute trajectories in complex EOF space, we take the timeseries described previously, EOF2 + i EOF1, standardize it, and low-pass filter it with a 40-day Lanczos filter (Boljka et al. 2018). Our conclusions are not sensitive to this choice.

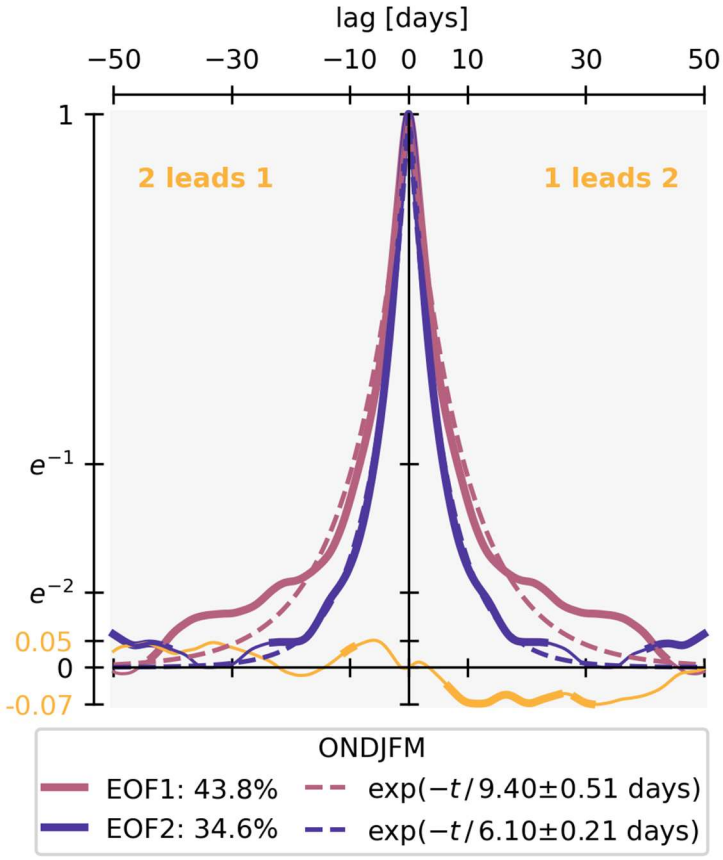

Figure S5: As in Figure S4a, but for October-March (ONDJFM).

After obtaining the filtered, complex EOF timeseries, we identify poleward propagating trajectories by computing the phase, separating the timeseries using the condition that there is a change in phase greater than ±340° within six hours, discarding trajectories shorter than 50 days, and discarding trajectories whose phase velocity is not positive. This final step ensures we have poleward propagating events and results in 41 trajectories from 1980-2023, shown in Figure S4b. The shading depicts the density of the trajectories, which show a dense annular shape around the origin, indicative of a gradual transition from EOF1 to EOF2 following a poleward propagation of the zonal wind anomalies. This suggests that the weak cross-correlations are due to a poor signal-to-noise ratio rather than the absence of propagation. Because propagation tends to prefer October-March, we repeat Figure S4a for those seasons in Figure S5. The cross-correlations are stronger at lags beyond 30 days than for the year-round data.

4. NAO Surface Impacts

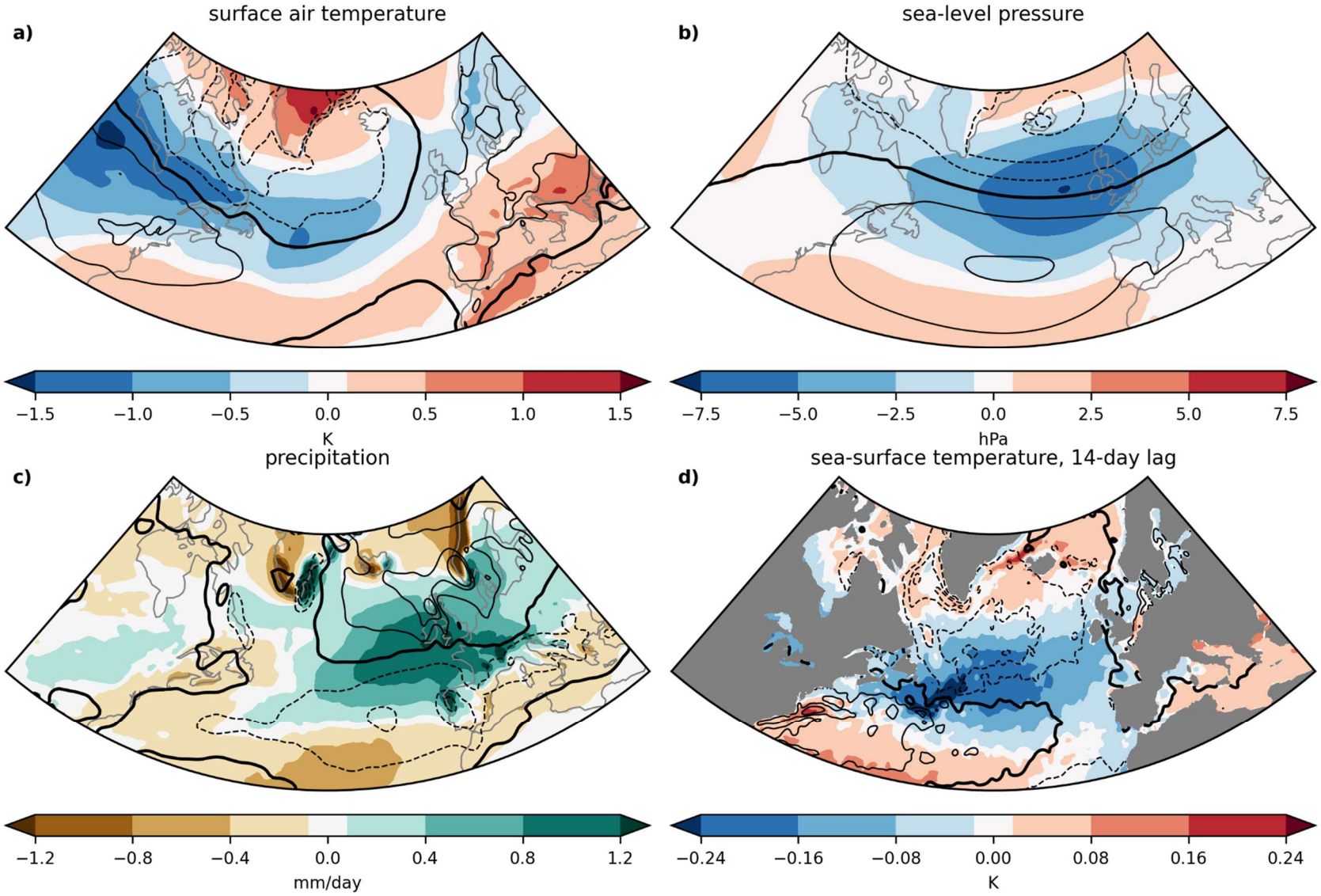

Figure S6: Surface variable response to positive NAO2 (shading) and negative NAO1 (contours), estimated through linear regression against each index from 1980-2020 using daily MERRA2 data and 1982-2020 using daily OISST data. The contour levels for NAO1 are the same levels used for the shading for NAO2. 950hPa temperature (a), sea-level pressure (b), and precipitation (c) are regressed at a 0-day lag to the NAO indices; sea-surface temperatures (d) are regressed at a 10-day lag. Only regression slopes significant at the 95% level are shaded. NAO1 and NAO2 follow convention, meaning that −NAO1 → −NAO2 → +NAO2 → +NAO1 corresponds to poleward propagation. The thick contour line represents the zero-line for NAO1. The region here depicts the region averaged over for the momentum budgets (100°W—30°E). ENSO is removed from the anomaly fields prior to regressing through a linear regression against the Multivariate ENSO Index.

Figure S6 shows the regression pattern between EOF2 (shading) and different surface climate anomalies. The EOF1 regression pattern (contours), classically viewed as the NAO pattern, has a zero-line at the location of the extrema of EOF2, meaning that they are in quadrature. Because EOF1 and EOF2 follow one another in phase space (Figure S4), these regression patterns follow one another in quadrature – in other words, they propagate poleward over time.

5. Expanded Predictability Analysis

The predictability analysis in Figure 4 compares the predictability of the propagating system to the classical assumption of uncorrelated, independently forced modes, which is captured by the Lorenz and Hartmann (2001) model. The increased predictability seen in the propagating system comes from two different sources which cannot be disentangled with the two cases already analyzed: non-normal dynamics and enhanced decay timescale.

The importance of the decay timescale can be illustrated by rewriting (5), uncoupled ($b_{ij} = 0$), as $\frac{dz_i}{dt} = -\frac{z_i}{\tau_{i,\mathrm{eff}}} + \widetilde{m}_i$, where $\tau_{i,\mathrm{eff}} = \frac{\tau_i}{1-b_{ii}\tau_i}$. Thus, since $|b_{ii}|\tau_i < 1$, $\tau_{i,\mathrm{eff}}$ is longer than τ_i for positive feedbacks ($b_{ii} > 0$) and shorter than τ_i when b_{ii} is negative. $\tau_{i,\mathrm{eff}}$ quantifies the new e-folding timescale predicted with the estimated linear feedback. Longer e-folding timescales correspond to more predictable systems. In this view, both timescales are lengthened from approximately 7 days to $\tau_{1,\mathrm{eff}} = 11.5$ days and $\tau_{2,\mathrm{eff}} = 8.5$ days for the propagating case (Table 1), and $\tau_{1,\mathrm{eff}} = 10.5$ days and $\tau_{2,\mathrm{eff}} = 7.9$ days for the non-propagating case.

However, in the propagating case, the modes are not independent; we must define the effective timescale matrix $\mathbf{T_{eff}} \coloneqq (\mathbf{I} - \mathbf{BT})^{-1}\mathbf{T}$, which is equivalent to $-\mathbf{A}^{-1}$ and thus not diagonal. However, it can be diagonalized using its eigenvalues $\lambda(\mathbf{T_{eff}}) = -1/\lambda(\mathbf{A})$, given by the negative reciprocal of (7), or $\mathrm{Re}[\lambda(\mathbf{T_{eff}})] = -\sigma^{-1} = 2\left(\tau_{1,\mathrm{eff}}^{-1} + \tau_{2,\mathrm{eff}}^{-1}\right)^{-1} = 9.7$ days. Thus, the decay timescale is the harmonic mean of the independent effective timescales, and it acts as the effective timescale for both modes when propagation is present. Compared to the non-propagating case, $\tau_{1,\mathrm{eff}}$ is 0.8 days shorter, while $\tau_{2,\mathrm{eff}}$ is 1.8 days longer. Thus, if we compare the decay timescales for the two cases using $\mathrm{trace}(\mathbf{T_{eff}})$, the decay timescale is about 5% longer in the propagating case, even though the e-folding timescales of EOF1 and EOF2 individually are the same (by construction).

The other source of higher predictability is the non-normal dynamics. To illustrate this effect, consider a stochastically-forced linear system like (1) with non-normal dynamics whose eigenvectors form a (non-orthogonal) basis. In this case, the dynamics $\mathbf{A}$ can be diagonalized (and thus, normalized) using its eigendecomposition $\mathbf{A} = \mathbf{V\Lambda V^{-1}}$. This means that our non-normal version of (1), when forced by a spatially uncorrelated forcing $\mathbf{f}$, can be transformed into a normal system through linear transformation of the state vector $\mathbf{p} = \mathbf{V^{-1}u}$ (Tippett and Chang 2003):

$$\frac{\partial \mathbf{p}}{\partial t} = \mathbf{\Lambda p} + \mathbf{V^{-1}f},$$

where the forcing $\mathbf{V^{-1}f}$ is now correlated across its modes. This explains why non-normal systems have higher predictability – the non-normality induces correlations between its normal modes, so that they are not excited independently, and thus their total predictability is greater than the sum of the predictability of each mode independently (Ioannou 1995).

To separate the combined influences of non-normality and decay timescale, Figure S7 expands the predictability analysis of Figure 4 with an additional method for removing propagation from the stochastic model, where we give EOF1 and EOF2 identical feedbacks resulting in the same decorrelation time as the propagating mode. This new case, “same eigenvalue”, is diagonal (and hence normal). Comparing it to the propagating case reveals the influence of non-normality independent of the decay timescale. Comparing the same eigenvalue case with the classical, non-propagating case reveals the role of the decay timescale, since both cases have normal dynamics.

Note that propagation does not strictly imply non-normality; the non-normality here is a result of the asymmetric cross-EOF feedbacks (Table 1). However, if one assumes the EOFs represent normal modes of A, the dynamics will be diagonal in EOF-space, and thus, normal. Diagonal dynamics do not have propagation. Thus, in the traditional assumption of no cross-EOF feedbacks and independent EOF1 and EOF2, the system is assumed normal, and its predictability is underestimated.

Figure S7a reveals that, at lead times less than two weeks, most of the predictability increase results from the larger decay timescale. However, two weeks later, the same eigenvalue case is directly between the two cases. This suggests that non-normality has a comparable effect to the increased decay timescale at longer leads.

We also examine the relevance of the predictability limit in Figure S7a for the internal predictive skill for each case in Figure S7b. This differs from Figure 4b, where both models aim to predict the propagating case. Figure S7b shows each model predicting itself in order to test whether the predictive advantage seen in Figure 4b stems purely from a prediction system which was ignorant of propagation. While the confidence intervals estimated for the skill overlap, suggesting there is no clear statistical advantage, the median skill lines follow the same hierarchy predicted by the theoretical limit in Figure S7a. Furthermore, the median skill in the propagating case is generally outside the estimated range for the classical case. We hypothesize that the increased predictability of the propagating system is at least partly due to the higher internal predictability demonstrated in Figure S7a.

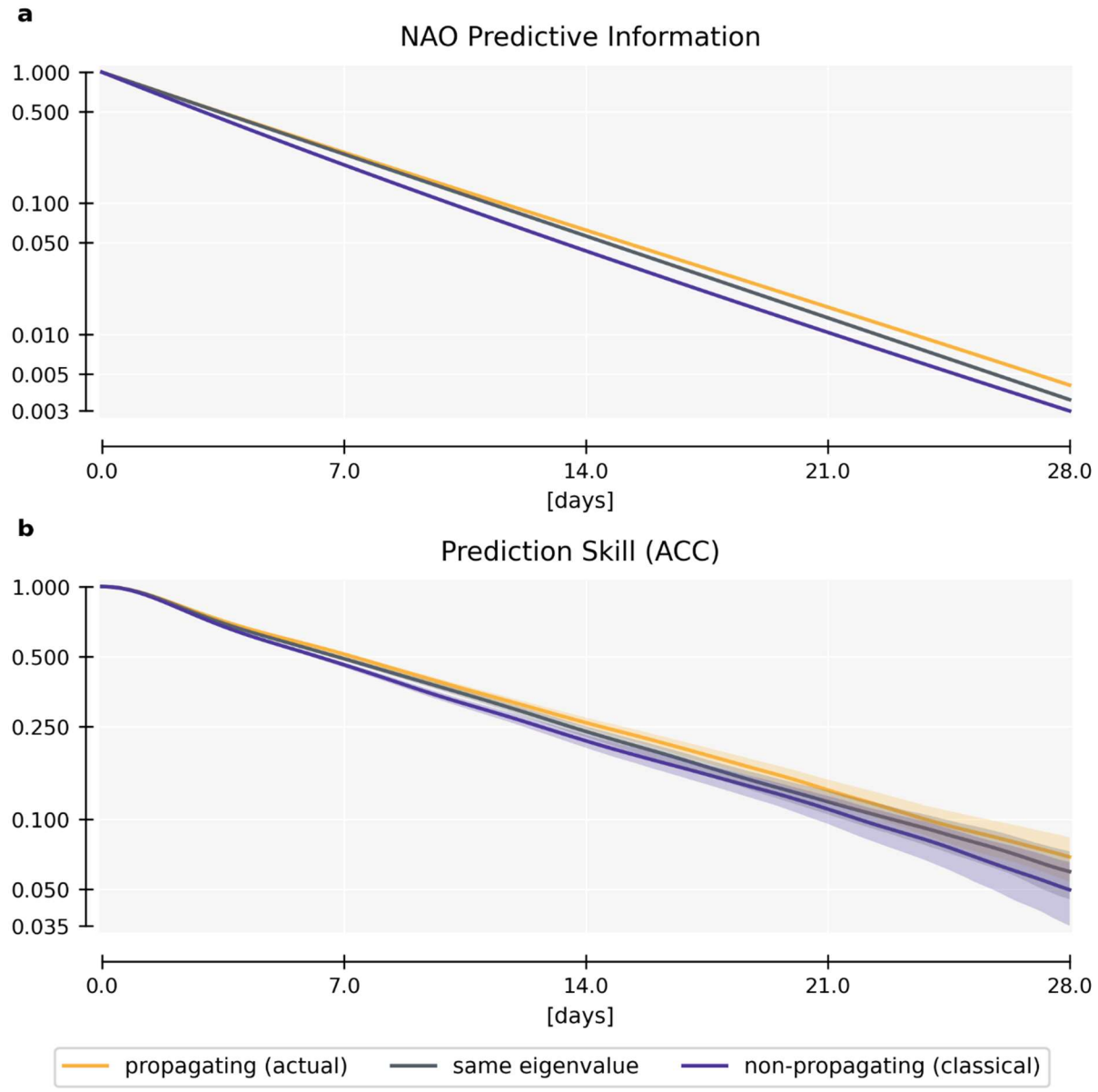

Figure S7: (a) As in Figure 4a, but including a non-propagating case with the same decay timescale as the propagating mode (same eigenvalue). (b) The prediction skill (anomaly correlation coefficient) between the stochastic model run using the dynamics matrices analyzed in (a) and their corresponding linear predictions. This differs from Figure 4b, where both cases are measured against the stochastic model driven by the propagating matrix.

6. DMD Validation

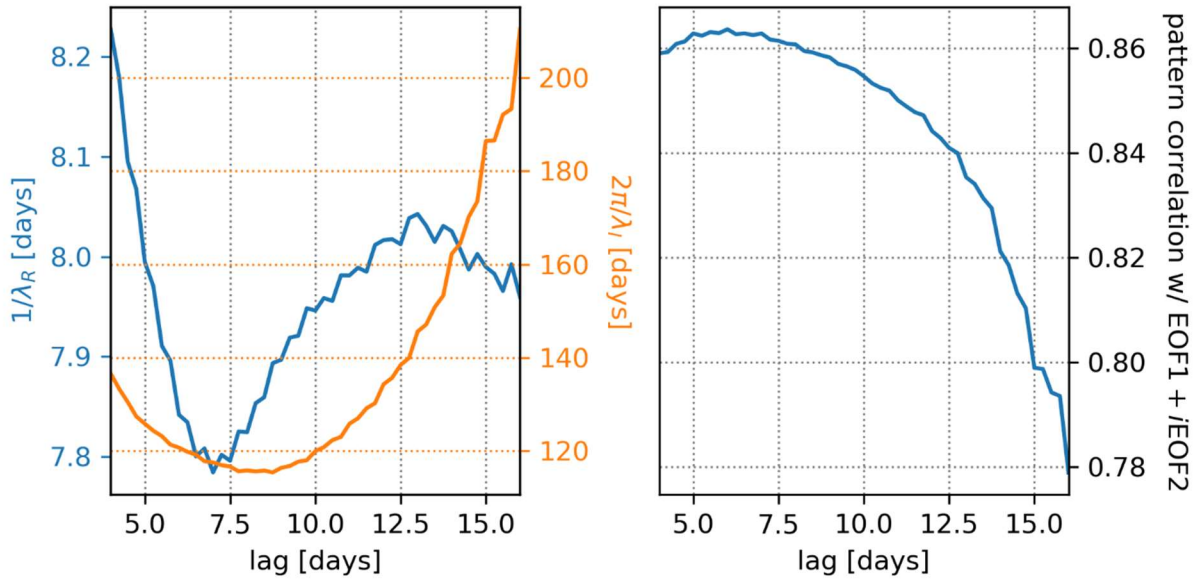

Figure S8: (left) Estimate of the eigenvalue λ for the least-damped, complex DMD mode as a function of lag. The decay rate (blue line) is given by $1/Re(\lambda)$, and the period (orange line) is given by $2\pi/Im(\lambda)$. (right) The pattern correlation between the leading complex DMD mode and the EOFs as a function of lag.

Figure S8 shows how the DMD eigenvalue corresponding to the NAO varies with the lag chosen for the lag covariance matrix, one of our free parameters (see Section 3.2). It also shows how the pattern correlation varies with lag. Generally, the lag should be greater than the synoptic timescale but not more than twice the mode's decay timescale, so we constrain this analysis to 4-16 days. Very short lags show higher pattern correlations but large variations in the eigenvalue, indicating they are too short for the assumptions underlying (3) to be valid. Longer decay timescales at longer lags mean the information contained in the mode persists longer, a sign that we are capturing more of the physics. However, the pattern correlation with the leading EOFs decreases at the same lags, suggesting we are not capturing as much of the variance. Thus, we choose an intermediate value (12 days) near the local minimum in λ_R (and thus a local maximum in $1/\lambda_R$) for the lag.

References

Boljka, L., Shepherd, T. G., & Blackburn, M. (2018). On the Coupling between Barotropic and Baroclinic Modes of Extratropical Atmospheric Variability. *Journal of the Atmospheric Sciences*, *75*(6), 1853–1871. https://doi.org/10.1175/JAS-D-17-0370.1

Lorenz, D. J., & Hartmann, D. L. (2001). Eddy–Zonal Flow Feedback in the Southern Hemisphere. *Journal of the Atmospheric Sciences*, *58*(21), 3312–3327. https://doi.org/10.1175/1520-0469(2001)058<3312:EZFFIT>2.0.CO;2

Lorenz, D. J. (2023). A Simple Mechanistic Model of Wave–Mean Flow Feedbacks, Poleward Jet Shifts, and the Annular Mode. *Journal of the Atmospheric Sciences*, *80*(2), 549–568. https://doi.org/10.1175/JAS-D-22-0056.1

Sheshadri, A., & Plumb, R. A. (2017). Propagating Annular Modes: Empirical Orthogonal Functions, Principal Oscillation Patterns, and Time Scales. *Journal of the Atmospheric Sciences*, *74*(5), 1345–1361. https://doi.org/10.1175/JAS-D-16-0291.1

Vallis, G. K., Gerber, E. P., Kushner, P. J., & Cash, B. A. (2004). A Mechanism and Simple Dynamical Model of the North Atlantic Oscillation and Annular Modes. *Journal of the Atmospheric Sciences*, 61(3), 264–280. https://doi.org/10.1175/1520-0469(2004)061<0264:AMASDM>2.0.CO;2